UNICA

UNIVERSITÀ
DEGLI STUDI
DI CAGLIARI

PhD Degree in Physics

XXXV Cycle

Sustainable Development of New Phosphors for Photonics Applications

Scientific Disciplinary Sector(s)

FIS/01

PhD Student Franca Chika, Ugbo

Supervisor Prof. Pier Carlo Ricci

Final exams Academic Year 2021/2022

Thesis defence: July, 2023

Dedication

This Project is dedicated to God Almighty the giver of knowledge and inspiration, the creator of all things. I am what I am today because He has made me. John 3 vs 27.

Acknowledgements

It is a great pleasure to see the hard work and dedication that I have allotted during all parts of my thesis come to light since I joined the Treetop Material Science and Spectroscopy Group. During that period, I had the opportunity to work with several people who have contributed in diverse ways to making this thesis successful in a delightful way academically and socially.

Before starting the presentation of my Ph.D. thesis, I would like to express my honest gratitude and sincere appreciation to all who have assisted and inspired me during my doctoral pursuit.

First, I am lucky to have Prof. Pier Carlo Ricci as the supervisor of my Ph.D. research. He is an amiable and kind-hearted person. I admire his aptitude and friendly personality. He has taught me how to do the research, go about the thesis work, and have shared a plentiful amount of time in conversation and on the procedure to finish the project in a short time. My special thanks go to Prof. Smet Philippe of Lumilab, Ghent University. For his help in discussion and his invaluable expertise gifted to me throughout my research stay. I like to offer my sincere appreciation to the professors in the Treetop materials Science and Spectroscopy group Prof. Carlo Maria Carbonaro, Prof. Daniele Chiriu, and Prof. Riccardo Corpino, for their support, time, guidance, and encouragement from the start of the study till the final version of my thesis.

I owe special thanks to all the people who have dedicated their time to help me out with the instrumentation needed to complete my thesis, Dr. Stefania Porcu, Dr. Jassica Satta, and Dr. Andrea Pinna of the Treetop material Science and Spectroscopy Group for their support, experimental knowledge, technical services, insightful advice, and discussion on the structural analysis and thermoluminescence, measurements.

The same appreciation goes to Dr. David VanderHeggen, Dr. Jieqi Hu, Dr. Zetian Yang, Dr. Verena Fritz, and Dr. Lisa Martins, who are members of the Lumilab Research Group, Ghent University, for their help with the spectrophotometer and discussions on luminescence materials.

I like to extend my gratitude to the members of the jury who have agreed to judge this thesis.

Throughout my Ph.D. life at Università degli Studi di Cagliari, the continuous and generous support from the members academic staff Prof. Paulo Ruggerone, Prof. Cappellini, Prof. Guido Mula, Prof. Michele Saba, Prof. Attilio Vittorio Vargiu, Prof. Bongiovanni, are greatly appreciated, I have known them during my first scholarship as a student under the international master's program (Erasmus Mundus) from 2016 to 2017. It was a great pleasure and honor to study and work with you.

I am highly honored to thank Prof. ABC. Ekwealor, Prof. F.I Ezema, Prof. D.N. Obiora, James Ezema and Omenihu Uloaku of NanoResearch group, Crystal Growth Lab, University of Nigeria, Nsukka, Nigeria. Your teachings, support, and encouragement made good impact on me.

Special thanks to my newly Ph.D. graduated co-researchers, Dr. Francesca Pisu and Dr. Chiara Oilla. Not forgetting my former colleagues at the office Dr. Moulika Hazra, Dr. Tullia David, and Dr. Saswati Bagchi. It was a pleasure to work with you all.

Last but not least, special thanks to my parents of blessed memory Mr. and Mrs Friday Ugbo, who have inculcated good virtues into my life and made sure I went to school at all costs, and to my lovely siblings for their undiluted support, prayers, and encouragement. I could not have been able to achieve this without you. I love and cherish you all.

Let me use this occasion to thank the amiable men of God whom their payers, has kept me going Rev. Gloria and Philcollins Obah, Pastor Dede Godspower, Pastor Richard, Dr. Pastor Ernest Ejeh, and Apostole Dr. Orinya Ejeh-Ochai. I sincerely appreciate all your prayers.

I must express my gratitude to Mr. and Mrs. Fillius Osubor, the Managing Director/CEO of Rinet Limited Lagos, Nigeria. Also, to Chief Dr. Chuks Okwuokenye, the Inneh of Owa Kingdom, and the proprietor of Calvary Polytechnic Owa-Oyibu, Delta State, Nigeria. For their kindness and encouragement.

There may be several others whom I have inadvertently left out. I seize this opportunity to thank all that indirectly or directly, have offered their helping hands in this thesis.

This thesis has been financed and supported by the PON-Ricerca e Innovatiozione. Thank you so much.

1.1. General Abstract

Phosphors with high efficiency, long afterglow (long persistent luminescent phosphor (LPLP)), crystalline and reproducible property for use in diverse application such as in sensor, storage, and lighting devices has become the central attraction of research in recent years. Different materials have characteristics that enable the achievement of this. As already established by previous studies, the method of synthesis affects the crystalline properties of a phosphor material. Therefore, very important to use a technique that will not require post-synthesis annealing for high yield. Mechano-luminescence (ML) is the emission of light by a phosphor through a mechanical activity that was carefully studied using the single impact method with different energy. In this research, various materials of plain calcium zinc oxysulfide (CaZnOS) and calcium gallium oxide ($Ca_3Ga_4O_9$ (CGO)) and their composites with Eu^{3+}, Tb^{3+}, Bi^{3+} Zn^{2+} were studied utilizing different synthesis routes. CaZnOS was carried-out for its high performance as a mechano-luminescent material, $Ca_3Ga_4O_9$ was for its great phosphorescence.

The materials studied in the first year of this research focused on the emission properties of CaZnOS crystals singly doped with Terbium and co-doped with Terbium and Europium. By studying the optical properties and the kinetics of recombination with time-resolved luminescence, the de-excitation mechanisms and the charge transfer processes have been established. A fundamental role is played by the defective centers and their efficient energy transfer process to the excited levels of Terbium, the mechanism being also active among co-doping rare earths (from Tb^{3+} to Eu^{3+}), allowing further tuning of the emission properties. Beside photoluminescence, the study shows that in case of mechanical stimulus as well, the mechano-luminescence follows the same path, where the defective states of the matrix efficiently excite the levels of dopants, producing a green emission at 545 nm from Tb^{3+} and a red emission above 600 nm from Eu^{3+}. Therefore, studying the relative ratio of dopants, it is shown how precisely tune across the visible part of the spectrum the mechano-luminescence emission.

The second year centred on optimizing the mechano-luminescent properties of CaZnOS: Tb using microwave-assisted synthesis (MAS) method. The results were compared with samples obtained through conventional solid-state methods. The analysis of the material's characteristics was accomplished using various techniques to investigate their structural, morphological, and optical properties. A detailed study of the material's mechanoluminescent properties was done through single impacts with varying energies. The results show that materials synthesized through microwave methods exhibit similar optical and, primarily, mechano-luminescent properties, making them suitable for use in photonics applications. The comparison of the microwave and conventional solid-state synthesis methods highlights the potential of

microwave-assisted methods to optimize the properties of mechano-luminescent materials for practical applications.

The third-year activity was done with CGO a long persistent luminescent phosphor (LPLP). The study involved careful synthesis and characterization of $Ca_3Ga_4O_9$: xBi^{3+}, yZn^{2+}, zTb^{3+} phosphors doped with different levels of Tb^{3+} ions. The aim of the investigation was to acquire an intense conception of the influence of Tb^{3+} doping on the optical and structural properties of the material.

overall, this study provides a comprehensive insight into the properties of long-persistent phosphors and demonstrates their potential for various technological applications, including optical data storage.

Generally, the study in this research with the different host materials such CaZnOS and $Ca_3Ga_4O_9$ and methods was done to adequately fulfil the requirements of the European Commission (EU) on this research by applying little amount of the rare-earth dopants such as (Tb^{3+} Eu^{3+}), for engineering, and construction of eco-friendly and sustainable new phosphors for photonics applications and develop new experimental methods to optimize the industrialization of photonic materials to decrease energy consumption.

1.2. **General Introduction**

In this era, modern materials contribute intensely to day-to-day living. Different technologies and technologically sophisticated devices such as wind turbines, solar panels, flat-screen television, modern cars, cell phones, digital and video cameras, computers, recording, and other electronic devices have come to life because of a series of materials such as cobalt, tantalum, lithium, molybdenum, and tungsten used in this manufacture. Hence the high need for these modern materials leads to the increased demand for these elements (Critical Raw Materials (CRMs)). CRMs are elements such as copper, cobalt, lithium, and re-earths which help actualize the manufacture of these modern devices and technologies that feed the increased demands for state-of-the-art technologies. CRMs and modern materials are inseparable. They go Pari per su with each other and are crucial for the efficiency of industries and the production of countless clean technologies and green applications. The role of critical raw materials cannot be over-emphasized as they have a significant deal of impact on our society, environment, and industries. The European Commission refers to CRMs as critical not because they are scarce resources but for their vast economic importance and the risk associated with their procurement compared with some other materials. Figure 1 presents the graph of supply versus economic importance of CRMs from the 2020

critical assessment. In the figure, CRMs are highlighted with red dots and are within the criticality region of the graph, whereas the blue dots are the non-critical materials.

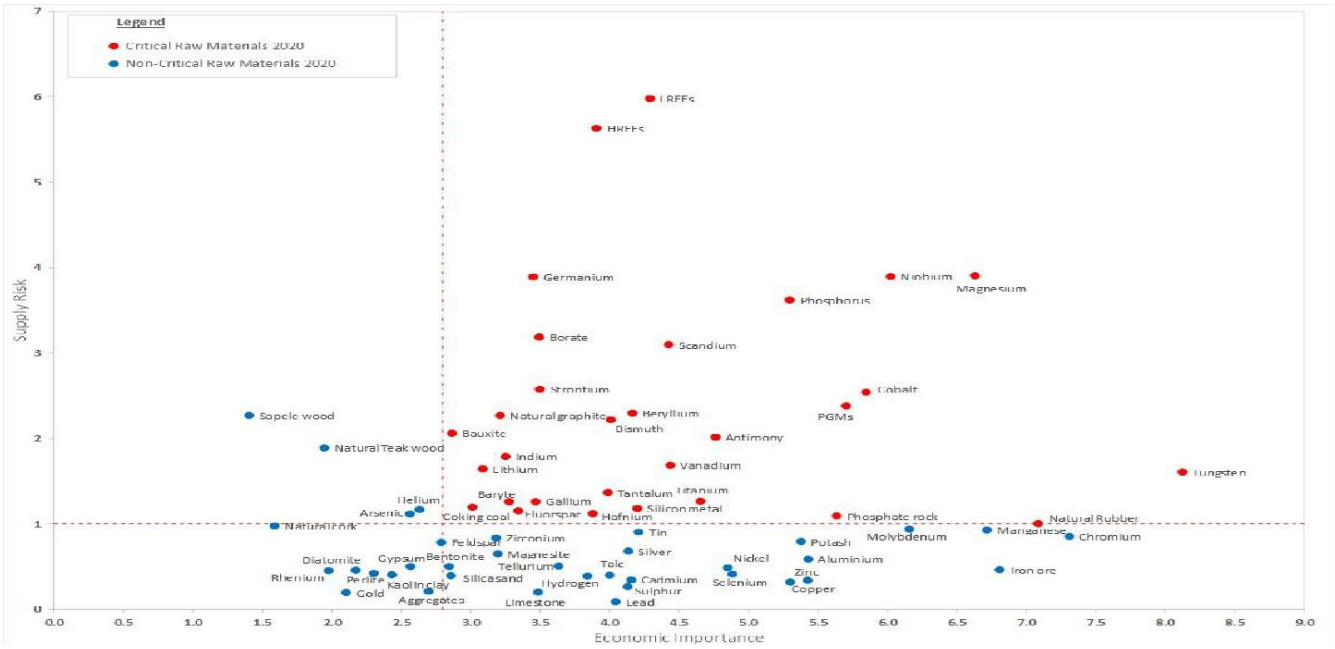

Figure1. 2020 Graph on the supply risk versus the economic importance of CRMs

Supply risk is overwhelmed by many factors. First is related to the fact that this vital material deposit is found in different parts of the world, and production is active only in a few, combined with governmental processes such as quotas, taxes, policies, and subsidies. Sadly, some continents do not have these mineral deposits and rely on others as their source. China as a nation has long been the pioneer supplier of these minerals to the world, and Europe depends on them as their source. China produces (magnesium, fluorspar, tungsten, germanium, antimony, gallium, graphite, indium, and rare earth). Several countries which also supply the CRMs in large amount includes Russia (platinum group metals), next is the Democratic Republic of Congo (tantalum, cobalt), and Brazil (tantalum and niobium). Often, production concentration problems emerge because of a lack of substitutes and recycling. Figure 2 outlines the recent production analysis of the world's 2020 CRMs supply as indicated by the European Commission (EC). The chart accounts that the largest share of CRM production comes from China, followed by Brazil, recording about 92% of niobium.

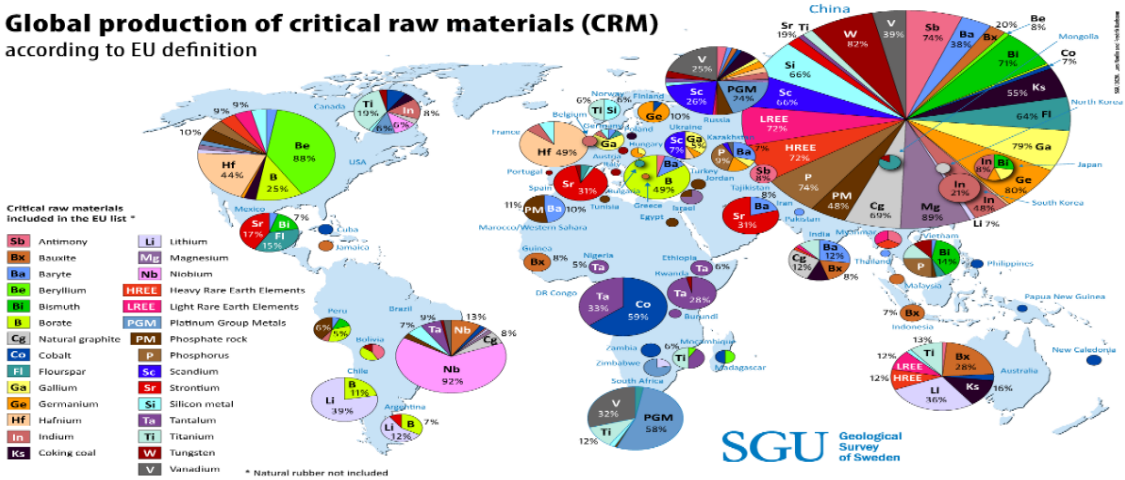

Figure 2. World production of the CRM as indicated in 2020 EC analysis.

Although the majority of the world's CRM is from outside of Europe, there are still a few deposits known to exist within Europe, for example, Sweden has cobalt, phosphate rock, PGE, fluorspar, REE, tungsten, and antimony. Secondly, the structure of response by various industries in the form of stockpiling, negotiating long-term agreements, or price hedging in the form of futures contracts could slow or hinder the supply of critical raw materials. Thirdly, increase in population, digitalization, industrialization, and high demand for raw materials from developing countries combined with the need to shift to a zero-carbon future affects supply. The Organization for Economic Cooperation and Development (OECD) forecasts that the 79 billion tonnes of present-day demand for CRMs will more than double to 167 billion tonnes by 2060. And that the world will require more materials in the coming years than the demands of today. There will be more dependency on raw materials than the way it is on oil.

The other measure of criticality is economic importance. Recent development has shown that the demand for raw materials will increase more and more in the nearest future due to high demands for new technologies and the drastic diffusion of major enabling technology. The German Federal Ministry of Economics and Technology predicted that new technologies would increase drastically by 2030. Strong measures are employed to determine the criticality of these materials in Europe, which entails the creation of critical raw material lists. The lists are consistently revisited every three years on the account to reflect the economy and the industries by the European Commission in conjunction with the Ad hoc Working Group on Defining Critical Raw Materials (AHWG). These lists are basically to serve the following purposes: contribute to enhancing the competitiveness of European industries following Europe's renewed industrial strategy; as well as increase the production of CRMs by boosting the extraction and reprocessing endeavours; another is to promote the efficiency and recycling of essential raw materials;

The list is also to help prioritize needs and actions for instance, it is a supportive component when negotiating trade agreements, challenging trade distortion measures, or encouraging research and innovation. Raw materials are of utmost importance to the European Commission, even though not listed among the critical ones, and their consistent supply is paramount. The first criticality list published in 2011 was drawn from the major concerns of the 2008 EU raw materials initiative to reveal production, market, and technological developments, and 14 elements were deemed critical. 20 and 27 raw materials were considered crucial for 2014 and 2017. The demands for raw materials kept increasing as the years went by, and 30 different materials were on the 2020 raw materials listed by the EC. These include Antimony, Beryllium, Baryte, Borate, Bismuth, Coking Coal, Cobalt, Fluorspar, Germanium, Gallium, Heavy Rare Earth Elements, Hafnium, Indium, Light Rare Earth Elements, Magnesium, Natural Graphite, Natural Rubber, Niobium, Phosphate Rock, Platinum Group Metals, Phosphorus, Silicon metal, Scandium, Tungsten, Tantalum, Vanadium, Lithium, Bauxite, Strontium, and Titanium, with strontium, Titanium, bauxite, and lithium new on the list. Due to a drop in economic importance, helium was not on the 2020 critical raw material list. As a result, the commission will continue to closely examine helium and nickel with changes relating to growing needs for storage devices.

Europe realizes the numerous applications, benefits, and vulnerabilities attached to the adequate flow of CRMs. Therefore, the priority of the EU as a highly industrialized nation is to secure unflinching and sustainable access to the supply of these raw materials for the well-functioning of its industries and the economy. European Union attained this by launching the Raw material initiative (RMI) in November 2008, whose duty involves three areas. Number one is securing sustainable access to materials within the EU and from outside of Europe. Number two is boosting the framework conditions for exploration, extraction, processing, and recycling of minerals within Europe, and thirdly, promoting actions on replacing rare-earth with substitutes. With these in mind, the European Commission, together with Europe leaders and the Members of the European Parliament, has raised a platform known as Horizon 2020 to create jobs and boost the economy. It is the largest research sponsoring body with over 80 billion Euros available budget that focuses on securing Europe's global competitiveness by aiding Science-based research to ensure Europe produces world-class Scientists, removes barriers to innovation, and make it easier for the public and private sector to work together in creating new ideas.

Investing in and supporting modern recycling is a critical activity of the RMI. Recycled waste can be infused back into the environment to support the economy and reduce the consumption of raw materials

while helping to avoid mining-related issues. The three waste flows covered by the EU comprise packaging, municipal waste, and electric electronic waste.

Another aspect is seeking alternatives to rare earths. Studies have shown that critical raw materials will soon be more important than oil and gas, the need to migrate to a carbon-neutral future, and the tremendous benefits to the industries and the economy. The demand for raw materials will be very high, and replacing rare-earth with substitutes will prevent mining and the excavation of lands in a quest for these valuable minerals.

This point is where this research has drawn its root. The research Sustainable Development of New Phosphor for Photonics Applications was carried out following the industrial doctoral scheme, under the auspices of PON-Ricerca e innovazione to undertake an experimental and applicative study on new materials for photonics without critical materials as defined by the European Commission. The project is in collaboration with LumiLab. Ghent University, Belgium, and FilarOptomaterials, Tortoli, Sardegna, Italy. Lumilab specializes in persistent luminescence synthesis and characterization. FilarOptomaterials is an industry that centers on the production of single crystals for photonic applications, where we have worked on the Raman data of laser materials. The research activity kick-started at the University of Cagliari with the Treetop Material Science and Spectroscopy Research Group.

The overall objective of the project involves:

- The study, engineering, and construction of eco-friendly and sustainable new phosphors for photonics applications, such as LEDs and CFLs with low or zero rare earth content (and CRM in general)
- Develop new experimental methods to optimize the industrialization of photonic materials to decrease energy consumption.

In other to accomplish these goals, different materials of plain calcium zinc oxysulfide (CaZnOS), calcium gallium oxide ($Ca_3Ga_4O_9$) long persistent luminescence phosphor (LPLP), and their composites using the dopants Eu^{3+}, Tb^{3+}, Bi^{3+}, and Zn^{2+} were synthesized based on the general properties already defined by previous studies, giving particular emphasis on the criticality of the elements defined by the European Commission. The materials synthesized were characterized partly at Treetop (X-ray diffraction (XRD), Raman, Time-resolved Luminescence spectroscopy and Mechanoluminescent (ML)), and at LumiLab (Photoluminescence (PL), Photoluminescence excitation (PLE), Scanning electron microscopy (SEM), Energy dispersive X-ray (EDX)) Ghent University.

The first-year activity was on CaZnOS: Tb^{3+}, Eu^{3+} already published. In the second year, the activities focused on applying a low-cost synthesis method with the microwave (Mw) in synthesizing Pure CaZnOS and doped with Tb^{3+}. The results were compared with the ones obtained with the solid-state synthesis method. Subsequently, the materials were characterized at the University of Cagliari with the Treetop group and LumiLab, (the collaborating University Ghent University) to check their structural, morphological compositional, and optical properties using the XRD, SEM, EDX, and Raman. The mechanoluminescent properties of the material were also extensively studied using a setup in the Treetop group with a steel ball released at various heights. The results obtained are analysed.

The third-year work centered on long persistent luminescent phosphor (LPLP) Ca3Ga4O9 of pure and doped with Eu^{3+}, Tb^{3+}, and co-doped with Bi, Zn. The doping percentage of Tb^{3+}varied at intervals, from 2% to a maximum of 8%, while Bi and Zn were held constant. The study was synthesized and conducted thorough characterization of $Ca_3Ga_4O_9$: xBi^{3+}, yZn^{2+}, zTb^{3+} (hereafter CGO) phosphors doped with different levels of Tb^{3+} ions. The analysis carried out includes XRD, Raman, Time-resolved luminescence, PL, and PLE to investigate their structural and optical properties. The main goal of this investigation was to gain a deeper understanding of the impact of Tb^{3+} doping on the optical and structural properties of the material. Overall, the study provided a comprehensive insight into the properties of long-persistent phosphors and demonstrates their potential for various technological applications, including optical data storage.

2.1. Introduction of CaZnOS doped with $Tb^{3+}$and Eu^{3+} prepared with only SS.

and CaZnOS doped with only Tb^{3+}prepared with SS and MW methods.

Phosphor is a solid material that releases light or luminescence in contact with radiation such as (ultraviolet light or an electron beam). Luminescence is the release of light produced by means different from heat. Luminescence is provoked by the movement of electrons into distinct dynamic states. Different kinds of luminescence exist according to the sources that excites them. For example, chemiluminescence excitation from a chemical reaction, photoluminescence excitation from UV light, mechanoluminescence excitation through mechanical activity, Bioluminescence excited from chemical reaction from living organisms, etc.

Phosphors could exhibit the characteristics of either phosphorescence or florescence depending on the defect levels in the material. For a fluorescence phosphor, the emission is primarily immediate and therefore typically only visible, when the light source is constantly on. while phosphorescent material can hold the absorbed light energy for some time and liberate light later, resulting in an afterglow that persists after the light has been turned off. Phosphorescence can last anywhere from a few seconds to hours.

In phosphorescence, an electron may be exhilarated, under reversal of its spin, to a higher energy state, known as an excited triplet state. Singlet ground states and excited triplet states have different multiplicities. For quantum mechanical reasons, transitions from triplet states to singlet states are forbidden and therefore the lifetime of triplet states is significantly longer than that of singlet states, i.e., the luminescence originating in triplet states has a far longer duration than that originating in singlet states. A triplet-singlet transition is much less possible than a single-singlet transition. The lifetime of an excited triplet state can be up to 10 seconds, in comparison with the 10−5 to 10−8 s average lifetime of an excited singlet state. Emission from triplet-singlet transitions can continue after initial irradiation. It persists longer i.e., greater than 10 to 8s, at times even seconds, minutes, and even hours. Several glow-in-the-dark materials, particularly toys, paints, etc., involve substances that accept energy from light and re-emit the energy again as light. These slower time scales of re-emission are associated with forbidden energy state transitions and hence these transitions occur less often in materials in which absorbed radiation may be released at a lower intensity for several hours. The Jablonski diagram describing fluorescence and phosphorescence is shown in figure 3.

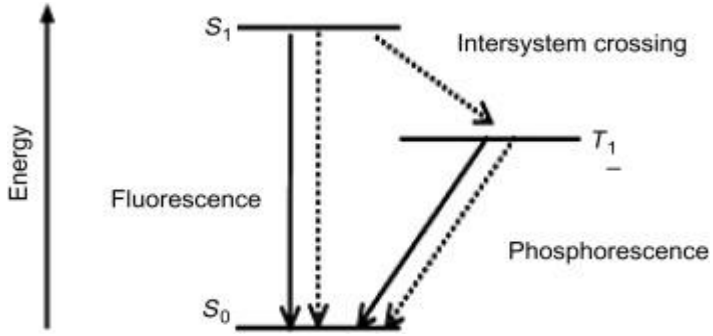

Figure 3. Schematics of the Jablonski diagram showing fluorescence and phosphorescence. Solid lines are radiative and dotted lines nonradiative transitions.

Photoluminescence provides a very important procedure for measuring the purity and crystalline quality of semiconductors and for quantification of the amount of disorder present in a system.

Many phosphors have been synthesized, has their distinct emission color and the period during which it emits light after stopping the excitation. Phosphors emit light by first absorbing radiation from a suitable source (X-ray, ultraviolet, chemical reaction, electron beam, and so on). The energy lifts the atoms in the material to an excited state, and then since the excited state is unbalanced, the material undergoes another transition back to the unexcited state, and the absorbed energy is released as light or heat. Diverse applications make use of phosphors. They are ubiquitous in state-of-the-art devices and technologies such as LEDs, CRTs, LCD screens, cell phones, wind turbines, computers, etc. Phosphors can be synthesized in the laboratory in the form of powder in such diverse ways as solid-state, microwave-assisted, sol-gel, solution combustion methods, etc.

In these recent times, CaZnOS has gained incredible popularity as a semiconductor matrix (host) among others such as nitrides and oxides not only for its ability to agree with a wide variety of rare-earth, metals, and non-metal dopants such as Mn, Eu^{3+}, Tb^{3+}, Co, Cu, Zn, Ce, but also for its high thermal, optical, and mechanical properties and suitable bandgap [1-3]. Studies have shown that the host has a lot of impact on the material. This is because the host crystals can absorb energy and transfer them to the dopant ions infused into the crystal lattice. CaZnOS possesses the characteristics of piezoluminescence. piezoluminscence is the ability of a material, particularly crystals, to produce light when triggered manually through vibration, sound, etc. The piezoeluminescence finds enormous use in applications

requiring stress to function. Some examples among many are the production and detection of sound, sparks used for kindling cooking gas, lighters, microbalance, etc. Piezoluminescence crystals exhibit mechanoluminescence characteristics.

Mechanoluminescence (ML) is a vital physical property of the CaZnOS powder material, where an emission of light is observed after a mechanical stress is applied [7]. Mechanoluminescent can be applied in many different phenomena as stress detection, light sources, encryption, etc. as shown in figure 4.

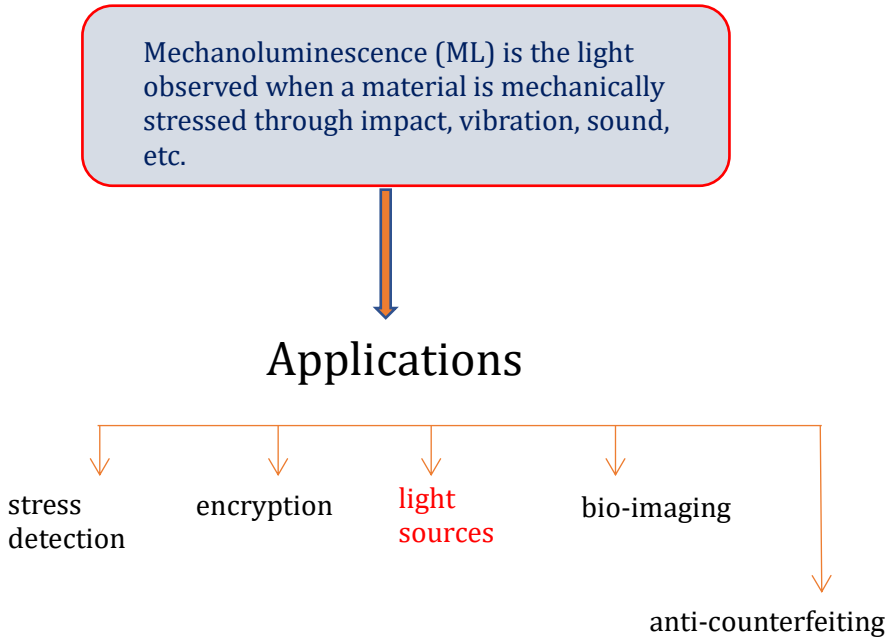

Figure 4. Mechano-luminescence and its applications

Many different solids such as metals, organic, ionic and glasses can exhibit the phenomenon of ML. ML is highly attractive for various applications such as sensors for stress, damage sensor, impact sensors, fracture sensors, and many more. The ML phenomenon can be adopted to explain the crack propagation in crystals, and mechanism of crack growth. In this study, the ML properties of pure CaZnOS doped singly with Tb^{3+}have been studied with a steel ball and set up with a retort stand and a hollow rod, with a glass sensor mounted under the hollow rod and a metre rule to measure heights. The steel ball was released at different heights starting from 30cm with an increment of 10 cm up to 100 cm. At measurements below 30 cm that is, 10 and 20cm, there was no ML noticed.

Several techniques have been adapted for the synthesis of CaZnOS phosphor. Many years of research have proved that the performing ability of a material is highly dependent on the synthesis procedure.

The solid-state synthesis (SS) is known from antiquity as a process of phosphor synthesis carried out in the laboratory, that involves activators and fluxes integrated into a host by grinding with mortar and pistol and heated in in the furnace at high temperature. The material is produced after stoichiometric calculation and weighing of the elements. The solid state is a great method of obtaining high crystalline phosphors powders that are useful in many applications. Another method that is capable of yielding phosphor powder of high luminescence is the microwave-assisted synthesis method (MAS). The MAS synthesis method is a very fast means of achieving phosphor powder. When compared with other methods such as solid-state, output results in a very quick time, without requiring further annealing of materials. A lot of researchers have used these methods to obtain different kinds of phosphor. In this work, the solid-state and the microwave-assisted synthesis methods were employed for the synthesis of pure CaZnOS and doped singly with $Tb^{3+}$and another doped with Tb^{3+}, Eu^{3+}.

Triply charged Terbium (Tb^{3+}) is a green emitting dopant, a member of the f-block element [5] that finds divers use in many applications including lasers, LEDs, exit signs and cathode-ray tubes, etc., because of the energy from its $^5D_4 \rightarrow {}^7F_J$ (where J = 3, 4, 5, 6) transitions. Its highest intensity peaks at 550 nm, with degradation time spanning from microseconds to milliseconds (μs -ms) [6].

The triply charged Europium (Eu^{3+}) is another beautiful red emitting activator that often shows the highest intensity at 617 nm that was used in this synthesis. It is used in a wide range of applications. When co-doped with Tb^{3+}in a suitable host produces great results [3].

In this work, we have incorporated both $Eu^{3+}$and Tb^{3+}into CaZnOS matrix using the SS and Mw synthesis methods while deliberately doping singly with $Tb^{3+}$with the aim to explore the beautiful green emission without any interference from any other dopants and doping with both Eu^{3+} and $Tb^{3+}$to enable adequate scrutiny of the results. The absence of rare earth elements in the host matrix and the very low concentration in the emitting centres of $Tb^{3+}$and Eu^{3+}, grants the sustainability of the phosphors with respect to the use of high content of critical raw materials.

As shown in Figure 5. CaZnOS aligns in a hexagonal symmetry and belongs to the space group P63mc (no.186) with structural parameters; a = 3.75470 Å, b = 3.75470 Å, c = 11.40140 Å, α = 90.0000°, β = 90.0000°, γ =120.0000°, V = 139.2000 Å^3 and Z = 2. Every Zinc (Zn) within the structure is tetrahedrally synchronised by three atoms of Sulphur (S), along with one atom of Oxygen (O), that is, ZnS3O connected with C3V point symmetry. The non-centrosymmetric structure of CaZnOS, having few similarities, constitutes levels of isotypic uneven hexagonal zinc sulphide (ZnS) and calcium oxide

(CaO) that are arranged in such a way that [ZnS3O] tetrahedrons are all aligned parallel, producing a polar structure [4].

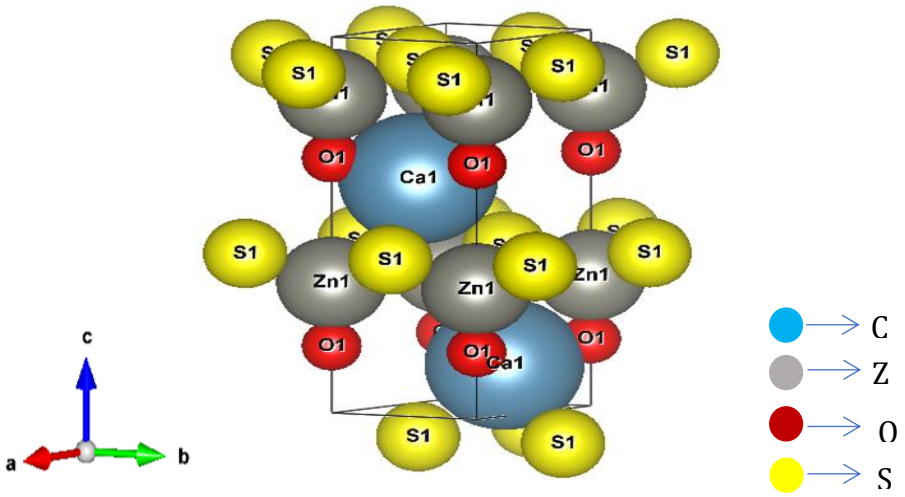

Figure 5. Crystal structure of CaZnOS

References

[1] Zhongxian Qiu, Chunying Rong, Wenli Zhou, Jilin Zhang, Chengzhi Li, Liping Yu, Shubin Liu, Shixun Lian (2013) A Strategy for Synthesizing CaZnOS: Eu^{2+} Phosphor and Comparison of Optical Properties with CaS: Eu^{2+}. Journal of Alloys and Compounds 583 (2014) 335–339.

[2] Abad Ellateef Abbass, HC Swart, and RE Kroon (2013) Effect of Ag nanoparticles on the luminescence of Tb^{3+}

doped sol-gel silica. SA institute of Physics. ISBN: 978-0-620-62819-8.

[3] Riccardo Corpino, Damiano Angioni, Jessica Satta, Franca Chika Ugbo, Daniele Chiriu, Carlo M. Carbonaro, Claudio Melis, Luigi Stagi, Pier Carlo Ricci (2021) Emission mechanism in single and co-doped Tb^{3+}: Eu^{3+}: CaZnOS Journal of Alloys and Compounds 868, 159007.

[4] Sambrook, T.; Smura, C. F.; Clarke, S. J.; Shi Halasyamani, P. (2007) Inorg. Chem., 16, 2571.

[5] P.C. Ricci, J. Satta, D. Chiriu, R. Corpino, C.M. Carbonaro, M. Salis, C. Melis,

P.S. Normile, J.A. De Toro (2019) Optical and vibrational properties of CaZnOS: The role of intrinsic defects. Journal of Alloys and Compounds 777, 225e233

[6] José Miranda de Carvalho, Cássio Cardoso Santos Pedroso, Matheus Salgado de Nichile Saula, Maria Claudia França Cunha Felinto and Hermi Felinto de Brito (2021) Microwave-Assisted Preparation of Luminescent Inorganic Materials: A Fast Route to Light Conversion and Storage Phosphors. Molecules, 26, 2882. https://doi.org/10.3390/molecules26102882

[7] Jonas Botterman, Koen Van den Eeckhout, Ives De Baere, Dirk Poelman, Philippe F. Smet (2012) Mechanoluminescence in BaSi2O2N2: Eu^{3+} Acta Materialia 60. 5494–5500

Emission mechanism in single and co-doped Tb^{3+}: Eu^{3+}:CaZnOS

Riccardo Corpino, Damiano Angioni, Jessica Satta, Franca Chika Ugbo, Daniele Chiriu,
Carlo M. Carbonaro, Claudio Melis, Luigi Stagi, Pier Carlo Ricci.
Journal of Alloys and Compounds 868 (2021) 159007
https://doi.org/10.1016/j.jallcom.2021.159007

2.2. Abstract

The study of new phosphors requires in-depth knowledge of the mechanisms and radiative emission paths and, with this aim, the study here reported focuses on the emission properties of CaZnOS crystals singly doped with Terbium and co-doped with Terbium and Europium. By studying the optical properties and, in particular, the kinetics of recombination with time-resolved luminescence, the de-excitation mechanisms and the charge transfer processes have been established. A fundamental role is played by the defective centers and their efficient energy transfer process to the excited levels of Terbium, the mechanism being also active among co-doping rare earths (from Tb^{3+} to Eu^{3+}), allowing further tuning of the emission properties. Beside photoluminescence, the study shows that in case of mechanical stimulus as well, the mechano-luminescence follows the same path, where the defective states of the matrix efficiently excite the levels of dopants, producing a green emission at 545 nm from Tb^{3+} and a red emission above 600 nm from Eu^{3+}. Therefore, studying the relative ratio of dopants, it is shown how precisely tune across the visible part of the spectrum the mechano-luminescence emission.

2.3. Introduction

Since the invention of the light bulb in the nineteenth century, the research of new materials and technologies has tried to feed the increasing lighting needs of the world. In the last decades, the extensive study of new inorganic luminescent materials suitable for lighting devices has become an area of sparking research interest, owing to some superior characteristics of these phosphors as compared to organic ones [1][2]. The main features include high stability, negligible thermal stress, novel green synthesis, efficient light generation, and long-life duration. Among the promising technologies for new lighting devices, mechano-luminescence (ML) is finding increasing attention because of its possible application in the field of pressure sensors and displays. It is well-known that luminescence is the emission of light due to the relaxation of excited electrons from the conduction band to the valence one in the case of

semiconductor materials [3]. Depending on the external stimulus that pumps the electrons in the excited states, one can appoint a specific luminescence phenomenon. ML is the emission of light produced after mechanical excitation of the material, because of an impact, the application of friction or pressure on the material or the formation of a crack (also known as tribo-, piezo and fracto-luminescence). Recently, ML was promoted for encrypted communication [4], information storage [5], patient care [6] and health monitoring [7][8]. Moreover, the absence of an external power generator opens new strategies for the creation of devices and applications like wearable devices, flexible displays, and electronic skin.

Different materials have been studied for ML effect, both organic and inorganic: in organic materials the mechano-luminescence effect is related to the aggregation-induced emission generated from an external stress [9]. However, this part of the research is at the beginning and only a very recent work tried to define a direct relationship between the external force strength and the emissive intensity [10]. In the inorganic materials the ML is in general related to the piezoelectric strain potential generated by strong electron-lattice coupling in the proximity of matrix defects. Up to now, the most studied ML material is the ZnS family, whose low efficient ML hampered any practical application. To achieve a market-ready development of this technique, designing and engineering new materials with a stronger ML efficiency than ZnS is required [11].

With this target in mind, calcium zinc oxysulfide (CaZnOS) has been studied in recent years as a promising ML material. First synthesized in 2007 [12], CaZnOS can be synthesized as a pure material or doped with activators. Activators are, in general, transition metals or rare-earth (RE) ions such as Eu^{3+}, $Tb^{3+}$and Ce, from lanthanides. By doping the host matrix with a very small amount of deliberately added impurity atoms, a significant change of the optical features is gathered in the doped crystal as compared to the ones of the pure host structure. As a consequence of the external stimulus, the activator may absorb the energy directly, leading to an electron jump from ground state to excited state, or the energy may be transferred from the host to the activator like the energy transfer reported in X-ray phosphors [13]. The general idea is to exploit the luminescence of the activators to enhance the optical features of the host material [14]. CaZnOS has been recognized as a semiconductor material able to host different activators owing to its suitable bandgap at 3.71 eV [15] [16], simple preparation procedure and excellent chemical stability [17]. CaZnOS has shown a great potential for applications in different technological fields, but the mechanoluminescent properties when doped with Mn give the most promising results. Indeed Mn: CaZnOS efficiently reacts to friction, compression, impact, and ultrasonic vibration with an efficient and

prompt emission, revealing its ability to detect and image diverse mechanical stimuli and demonstrating its practical potential application as stress sensors [17].

Beside Mn doping, recent works have shown ML effect also from CaZnOS host doped with different REs, achieving good ML performances in Tb^{3+}doped samples [18] [19]. Tb^{3+} activator typically emits an attractive green light that is generally exploited in LEDs and gigantic light colour screens. The green light is emitted because of the intensities of the four peaks originating from the $^5D_4 \rightarrow {}^7F_J$ (J = 3, 4, 5, 6) transitions, the peak with the highest intensity occurring close to 550 nm [14] [20]. However, to increase this green luminescence efficiency and possibly tune it, the general approach is to exploit energy transfer from sensitizers to Tb^{3+} in a suitable host. In lighting devices, the Europium ion exhibits unique absorption and emission efficiency in different hosts and, importantly, Eu^{2+} is an excellent sensitizer for Tb^{3+} ion [21], whilst Tb^{3+} ions work as sensitizer for Eu^{3+} [22]. In addition, a colour tuneable luminescence can be achieved by changing the doping ratio of REs [21]. Interestingly, the study on the luminescence properties and the energy transfer mechanisms of Tb^{3+}: Eu^{3+} co-doped CaZnOS has not been reported lately.

In this work, we employed CaZnOS as the host to exploit its suitable crystallographic sites for Eu^{3+} and Tb^{3+} ions doping in the crystal. Several synthesis techniques have been recognized for preparing CaZnOS powders, including solvothermal [23], co-precipitation [24], solid state reaction [25], hydrothermal [26], microwave [27]. In the present paper the structural and optical characterization of solid state synthesized Tb^{3+} doped, Eu^{3+} doped and Eu^{3+}: Tb^{3+} co-doped CaZnOS samples are presented and the kinetics of the recombination processes from the excited states are analysed. The analysis of the absorption and excitation spectra of the luminescence, coupled with the steady state and time resolved measurements, define the presence of non-radiative paths among defects to RE elements and between RE ions to RE ions. Finally, single impact mechanoluminescent measurements were performed, to prove the efficient effects in the co-doped CaZnOS samples, and a general model of the energy transfer is elucidated.

2.4. Experimental

Samples were prepared by solid-state synthesis starting from $CaCO_3$, ZnS, Eu_2O_3 and Tb_4O_7 powders. First, pure CaZnOS was obtained by the solid-state reaction as depicted by equation 1.

$$CaCO_3 + ZnS \rightarrow CaZnOS + CO_2 \quad (1)$$

The powders, in stoichiometric ratio, were mixed in an agate mortar, transferred in an alumina crucible, and then sintered in a tubular furnace under constant flow of nitrogen gas (N_2). The temperature was slowly increased up to 1000°C with a 10°C/min ramp rate and maintained constant for 5h. Then, the samples were naturally cooled down to room temperature. The same procedure was applied to synthesize doped and co-doped samples, according to the following equation 2.

$$(1\text{-}x\text{-}y)\ CaCO_3 + ZnS + x/2\ Eu_2O_3 + y/4\ Tb_4O_7 \rightarrow Ca_{1\text{-}x\text{-}y}ZnOS{:}\ xEu,\ yTb + CO_2 \qquad (2)$$

In the case of doped and co-doped samples, Li_2CO_3 was necessary for charge balance purposes and as reaction catalyst [28] [29]. Indeed, Eu^{3+} and Tb^{3+} RE ions have larger charge states than Ca^{2+} and Zn^{2+} ions they are substitutional to. So, on average, two Ca or Zn sites should be substituted by a RE dopant and a Li ion. The produced samples, except for pure CaZnOS, contain various quantities of dopants, Eu^{3+} only (1%, 3% and 5 wt%), Tb^{3+} only at the percentage of 5 wt% and Eu^{3+} and Tb^{3+} with fixed quantity of 5 wt% Tb^{3+} and 1%, 3% and 5 wt% of Eu^{3+}.

The crystalline phase was characterized by means of X-ray powder diffraction. X-ray patterns were collected by using a Bruker D_8 advance diffractometer with $\theta - 2\theta$ Bragg-Brentano geometry with Cu K_a radiation at room temperature.

To carry out quantum-mechanical calculation, we performed simulations within the pseudopotential planewave method (PWSCF) included in the Quantum- Espresso distribution, based on density-functional theory (DFT), periodic-boundary conditions, plane-wave basis sets, and pseudo-potentials to represent the ion-electron interactions [30]. We used the generalized gradient approximation (GGA) in the Perdewe Burkee Ernzerhof (PBE) version [31] for the exchange correlation potential and ultrasoft pseudopotentials [32]. The electronic Kohne Sham wave functions were expanded using a plane wave basis set, up to a kinetic energy cut-off of 35 Ry. Monkhorst-Pack grids were used to sample the Brillouin zone, 8x8x8-point was used. We calculated the Raman and IR spectra of using Density Functional Perturbation Theory (DFPT) [33], as implemented in the quantum-espresso package.

Raman measurements were carried out in backscattering geometry using 532 nm line by a wavelength stabilized diode module (Lasos GLK 532 laser) coupled with a Reflecting Bragg Grating (Optigrate-Braggrade 532) to narrow the laser line. Measurements were performed at room temperature with a triple spectrometer Jobin-Yvon Dilor integrated system with a spectral resolution of about 1 cm^{-1}. Spectra were recorded in the Stokes region by a 1200 groove/mm grating monochromator and a LN-cooled charge coupled device (CCD) detector system.

Steady state photoluminescence measurements were performed using the filtered light from a laser driven Xenon lamp (EQ- 99X) with a final bandwidth of about 1 nm. The emitted photoluminescence was collected by means of an optical fiber connected to an Avantes Thermo-Electric Cooled spectrometer.

The mechanical pulse for the mechano emission, was generated by a stainless-steel ball (10 mm diameter, 8.5 g) at a speed of 4 m/s (measured with Airsoft E9800-X anemometer) on a thin powder layer of sample (about 0.5 mm). The impact zone was placed on a CaF_2 transparent substrate, and the emitted light was collected from the opposite part with respect the direction of the ball and it is focalized on a gateable intensified CCD (PI MAX Princeton Inst.).

Time resolved luminescence measurements were performed using an optical parametric oscillator with a frequency doubler device, pumped by the third harmonic (355 nm) of a pulsed Nd:YAG laser (Quanta Ray Pro 730). The excitation pulse width at half-maximum was 8 ns with 10 Hz of repetition rate, and spectral bandwidth less than 0.3 cm^{-1}. The collected signal was dispersed by a spectrograph (Arc-SpectraPro 300i) with a spectral bandpass <2.5 nm and detected by a gateable intensified CCD (PI MAX Princeton Inst.). To minimize the dark current, the detector is cooled to -20 °C by a Peltier device.

2.5. Results and Discussion

The X-ray diffraction patterns of Eu^{3+} doped, Tb^{3+} doped and Eu^{3+}/Tb^{3+}doped materials were analysed by means of the software MAUD [34] as depicted in Figure 6. The main phase was determined to be CaZnOS structure (ICSD card no. 245309), with some traces of reactants oxides: CaO and Tb_2O_3 for samples containing Tb^{3+}. Eu_2O_3 was not detected in Eu^{3+}containing samples and co-doped ones, showing that its presence is below the detectability of the instrument.

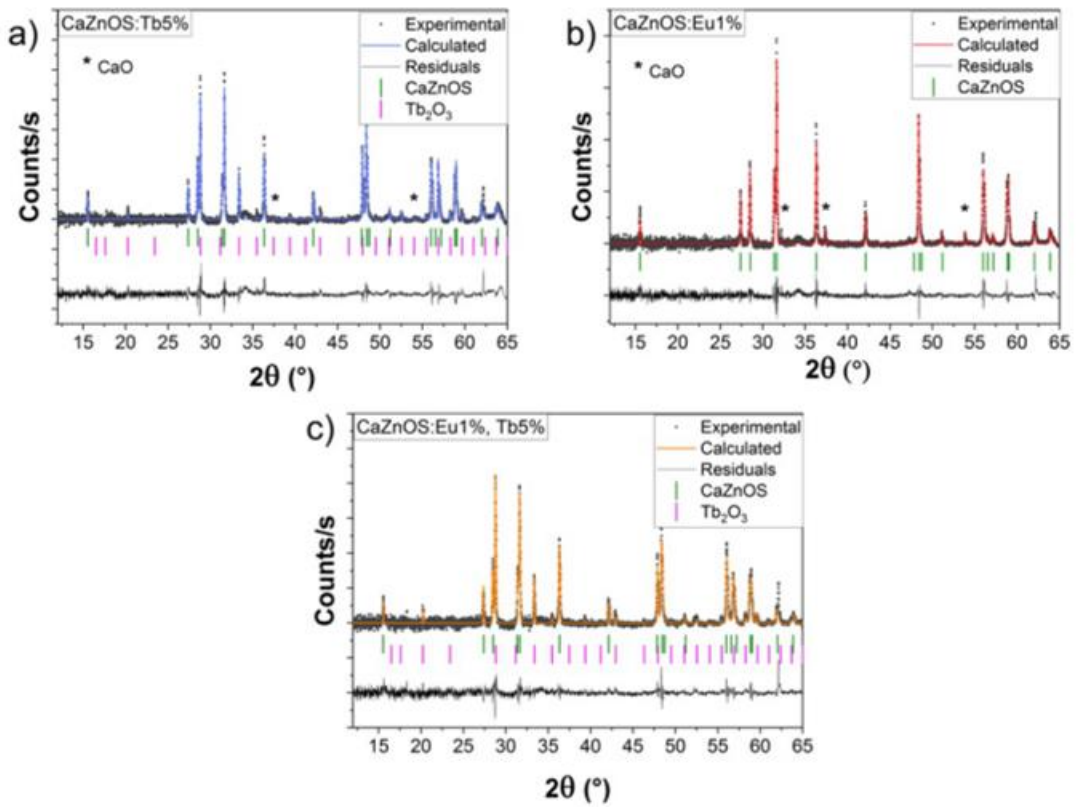

Figure 6. X-ray patterns of CaZnOS: Tb^{3+}5%, CaZnOS: Eu^{3+}1% and CaZnOS: Eu^{3+}1% Tb^{3+}5%.

The Raman analysis provides a deeper study of the structural properties of doped samples. Figure 7a compares the Raman spectra of Tb^{3+}doped and pure CaZnOS. The indicated bands are characteristic of CaZnOS structure [25] and the broadening and peak shift observed for doped samples (as highlighted in the inset) shows that the investigation of the doping process can be pursued with a detailed analysis of different characteristic Raman bands. Indeed, the region in the range 50 cm^{-1}-150 cm^{-1}, related to bound heavier elements, presents some spectral changes in the case of Tb^{3+}doped sample, regarding both the peak position and the width of the vibrational modes at 75, 102 and 124 cm^{-1}, that can be related to the Tb^{3+} substitution process within the undoped structure.

To quantitatively investigate the effect of doping on the measured Raman bands, a fit on each single band was carried out by means of a pseudo-Voight fitting function:

$$f(x) = A\left[m_u \frac{2\varpi}{\pi 4(x-x_c)^2+\varpi^2}\right] + (1-m_u)\frac{\sqrt{4ln2}}{\sqrt{\pi}\varpi} e^{-\frac{4ln2}{\varpi^2}(x-x_c)^2} \quad (3)$$

where A is a scale factor, m_u the weight factor between the two curves (Lorentzian and Gaussian) composing the Voight profile, ω is the full width at half maximum (FWHM) of the curve and x_c is the curve's centre x coordinate, i.e., the Raman shift in the present case.

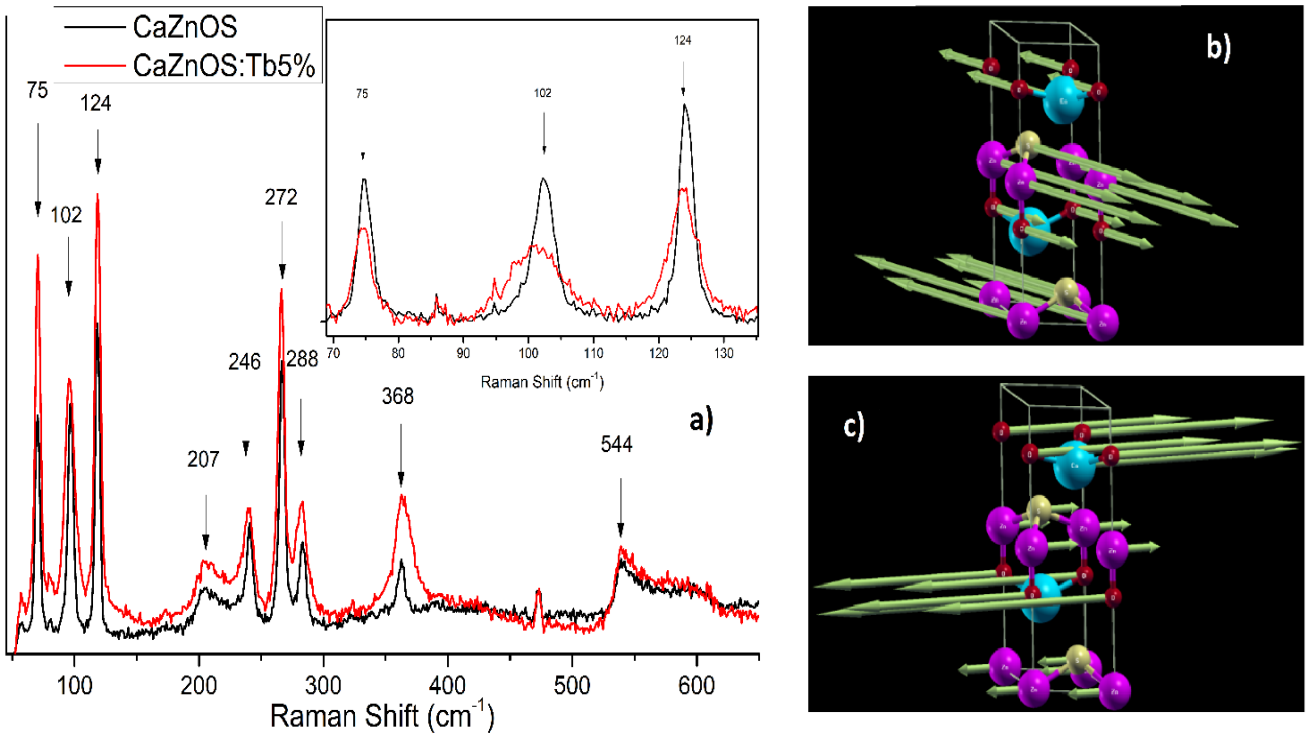

Figure 7a) Comparison between Raman spectra of pure CaZnOS and CaZnOS: Tb^{3+}5% and magnification of the region 70-140 cm^{-1} and results of DFT simulation for E_2 modes, i.e. bands at 75cm^{-1} b) and 102 cm^{-1} c) . Light blue: Ca, Purple: Zn, Red:O.

Table 1 reports the measured position of the peaks and the computed features of fit resulting parameters for Raman bands. The m_u coefficient represents the percentage of Lorentzian contribution with respect to the Gaussian one. It is well known that a physical process that has the same probability of occurrence for all the molecular units in the system produces a Lorentzian line shape (homogeneous broadening), while if it has a random distribution of occurrence an inhomogeneous broadening is produced, Gaussian line curve being the suitable distribution in this case. The high percentage of Lorentzian contribution in all the samples strongly indicates a rigid crystallinity structure of the samples. The analysis of the experimental data, supported by DFT simulations, enables the determination of the main substitution site for dopants: Figure 7b and 5c represents the oscillations associated with the bands at 75 cm^{-1} and 102 cm^{-1} (E_2 like modes) in pure CaZnOS as obtained by DFT calculations [25]. The latter largely depends

on the oscillation of Ca (Figure 7c), and its position is shifted to 100 cm^{-1} in the Tb^{3+} doped samples. On the contrary, the band at 75 cm^{-1} remains cantered at the same Raman frequency in the doped sample and its representation shows the low dependence on Ca ions' oscillations (Figure 7b). This consideration clearly supports the idea that the main substitution site is Ca rather than Zn for Tb^{3+}ion, according to their larger ionic radius (99 pm and 74 pm for Ca^{2+} and Zn^{2+}, respectively, the Tb^{3+} ionic radius being 94.7 pm).

Sample	x_c (cm^{-1})	m_u	ω (cm^{-1})
CaZnOS	75	0.8	2.5
	102	0.9	3.8
	124	0.7	2.6
CaZnOS: Tb^{3+}5%	75	0.7	3.1
	100	0.8	9.6
	124	0.9	5.0

Table 1 resulting fit parameters for Raman bands.

A similar analysis was not possible on Eu^{3+}doped and co-doped samples due to the luminescence induced by the 532 nm laser used for high resolution measurements. Raman spectra of that kind of sample were obtained by a different Raman apparatus (lower resolution and 1064 nm laser as exciting source) that confirmed the CaZnOS structure. Due to the lower spectral resolution, it was not possible to make further claims about the substitutional site. However, the Eu^{3+} ionic radius (98 pm) is like the one of Tb^{3+} ion and it is possible to assume that the substitutional site remains the same.

Previous studies on CaZnOS crystals reported band gap values ranging in the 3.5-4.0 eV [35], [36]. Recently, Zhang et al. [19] estimated 3.88 eV (i.e., 320 nm), reporting that the band gap evaluation is affected by the presence of intrinsic defect sites. Indeed, the absorption band enlargement to lower energies has been attributed to oxygen vacancies, claimed to be responsible for the optical properties of the intrinsic material [25]. Figure 8 depicts the steady state photoluminescence (PL) spectra excited at 320 nm. The pure CaZnOS spectrum shows a broad band centred around 500 nm, associated with oxygen vacancies [37]. When doping with Eu^{3+} and co-doping with Eu^{3+} and Tb^{3+}, the dopants produce a change in the overall optical emission of the host, the presence of dopants being evidenced by the narrow lines

in the PL spectra. The narrow emission at 545 nm is related to the recombination from the $^5D_4$ excited levels to the $^7F_5$ ground states of Tb^{3+}. The emissions above 600 nm are related to the recombination at the Eu^{3+} sites.

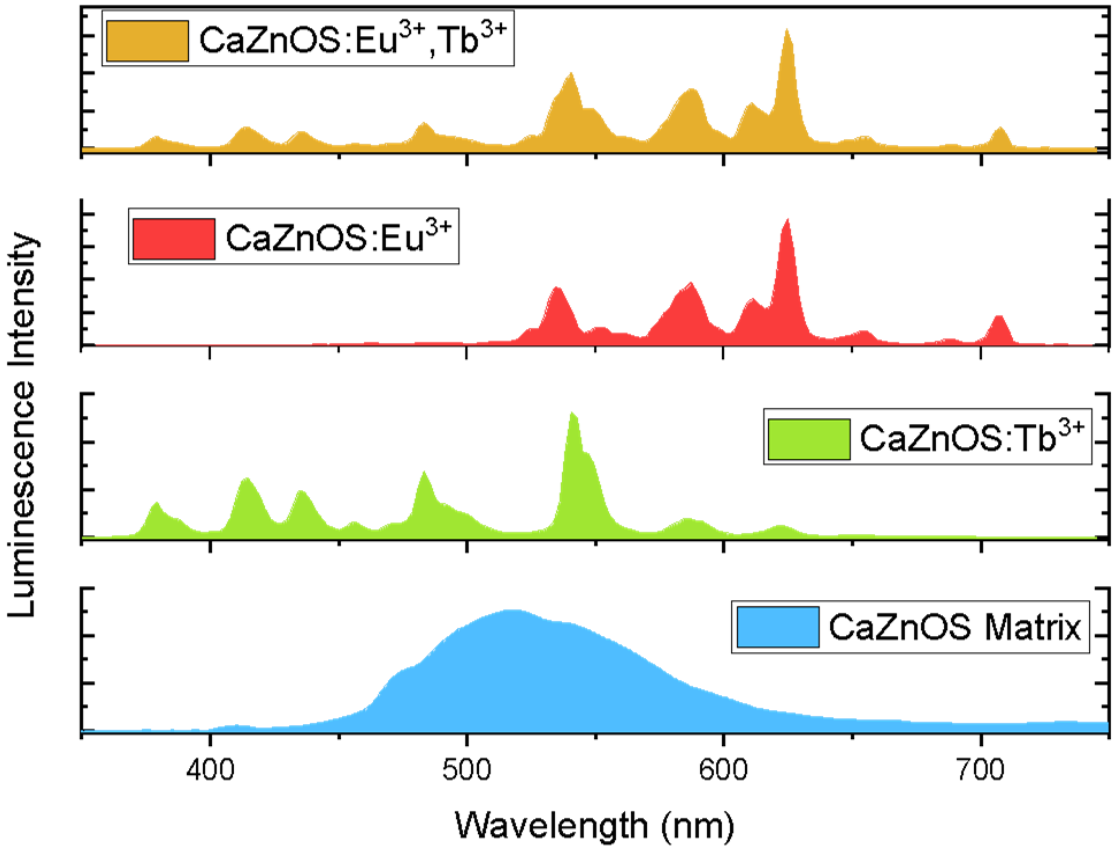

Figure 8. Steady time Luminescence spectra for intrinsic CaZnOS, Eu^{3+} doped and Eu^{3+}: Tb^{3+}: co-doped CaZnOS with excitation at 320 nm.

To investigate the photoluminescence dependence on the excitation wavelength, photoluminescence excitation measurements (PLE) were performed. The spectra of the single doped samples, reported in figure 9, clearly show several bands, due to the matrix and to the rare earth dopants.

The PLE evidences the presence of sub-bandgap excitation paths that recombine in the broad band [25]. It is also evident that such levels populate the excited levels of the rare earths. The recombination $^5D_4 \rightarrow {}^7F_5$ of Tb^{3+} ions (emission band at 545 nm) are populated mainly at 370 nm (Figure 9a). The Eu^{3+} emissions can be easily monitored following the band at 625 nm. This recombination is excited almost

uniformly from about 300 nm to 390 nm, with a minimum at about 370 nm (figure 9b). Hence, a key point that emerges from the PLE spectra can be outlined from the analysis of the recombination of Eu^{3+} centers. The effect of the co-doping process is to extend the excitation range of this emission (625 nm) down to 270-280 nm and to smooth the minimum at 370nm (figure 9c). The comparison with the spectrum of the sample single doped with Tb^{3+} (figure 9a), strongly suggests that the recombination at the Eu^{3+} centers are excitable at the Tb^{3+} sites.

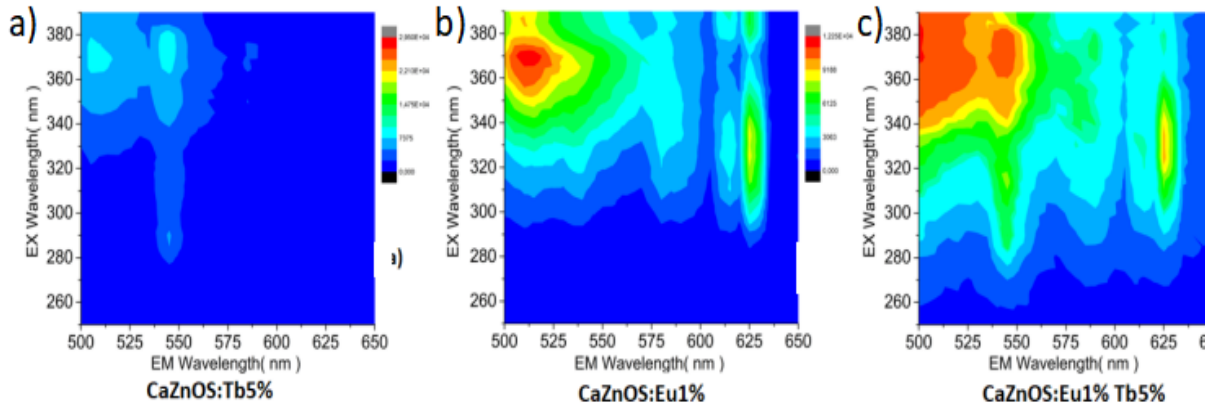

Figure 9 2D-Photoluminescence excitation spectra of CaZnOS doped with a) 5% Tb^{3+}, b) 1% Eu^{3+} and c) 1% Eu^{3+} 5% Tb^{3+}

Time resolved luminescence gives more insights on the optical properties of the investigated material and about the kinetics of the radiative paths. The analysis of time-resolved measurements at room temperature showed multiple emission bands in the blue, green and red region with complex kinetics ranging from nanoseconds to milliseconds time-domain. The luminescence contribution from the matrix, already assigned to defects related centres [25], is represented by the broad band centred at about 500 nm. Figure 10 evidence the very fast contribution from the defects in the co-doped sample, where after 100 ns (delay pulse) the broad band is almost totally absent and only narrow emissions, typical of the RE elements, are observed. Considering that the decay time in pure CaZnOS matrix is normally much longer than this time scale (ranging from microseconds to milliseconds), this result strongly indicates that the intrinsic levels of the matrix possess very efficient non-radiative energy transfer processes to the radiative channels of the doping element.

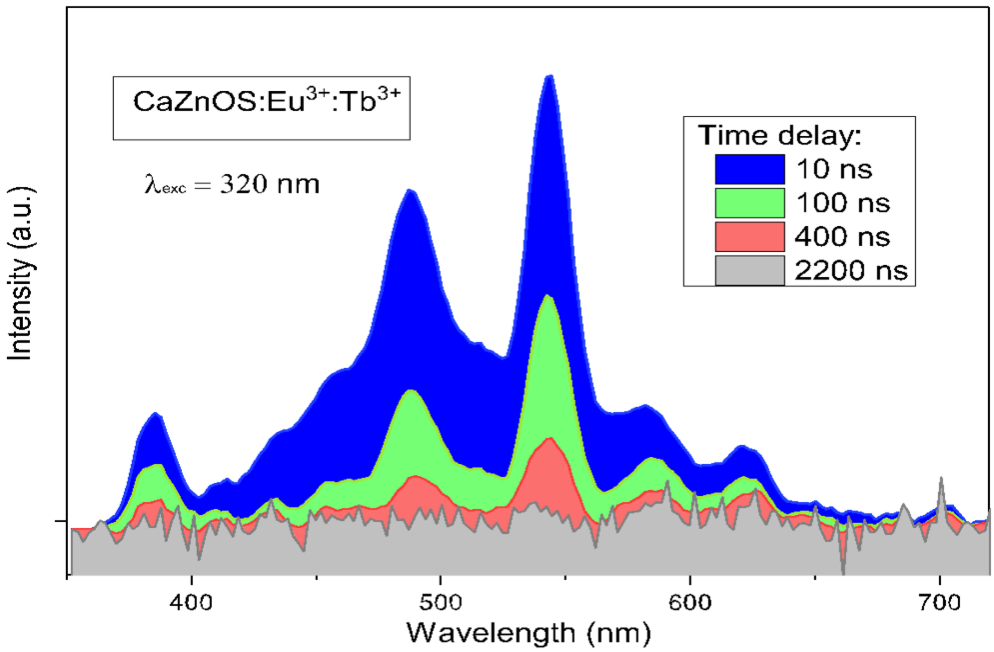

Figure 10. PL emission of CaZnOS: Eu3+$^{3+}$-Tb^{3+}samples recorded at different time delays.

Figure 11. underlines the different lifetime of 540 nm line of Terbium as a function of Europium doping percentage. The data were fitted with a sum of two exponentials for the Tb^{3+} containing sample and with three exponentials for the co-doped samples.

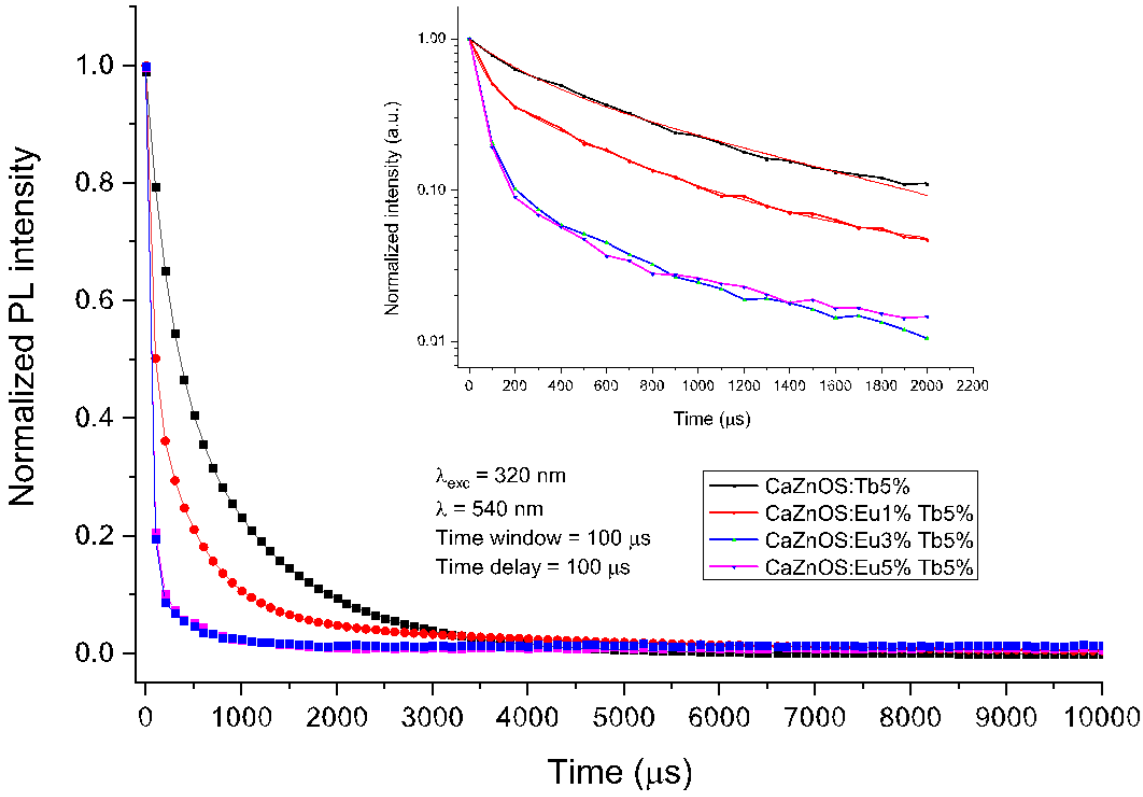

Figure 11. Time decay behaviour of co-doped Tb^{3+}: Eu3+: CaZnOS for different co-doping percentages.

The inset focuses in a semi-log scale the time window to highlight the different behavior as a function of the relative co-doping percentages. The characteristic times that emerge from this analysis are respectively of the order of tens of microseconds, hundreds of microseconds, and milliseconds [25]; the last two were characteristic of the Tb^{3+} containing sample, while the faster component arose after the insertion of Eu^{3+}. To have a quantitative and unique reference number relative to this kind of analysis, an average lifetime was computed using the following relation [38]:

$$\tau = \frac{\int_0^T I(t) \cdot t dt}{\int_0^T I(t) dt} \quad (4)$$

Where I(t) is the time-dependent photoluminescence intensity. This also allows calculating the transfer efficiency by the relation:

$$\eta = 1 - \frac{\tau}{\tau_0} \quad (5)$$

Where τ_0 is the average lifetime of the activator (Tb^{3+}) in absence of the sensitizer Eu^{3+}. The computed results are shown in table 2:

Excitation line	320 nm	
Sample	τ [μs]	η [%]
CaZnOS: Tb^{3+}5%	634,35 ± 0,10	-
CaZnOS: Eu^{3+}1%, Tb^{3+}5%	551,26 ± 0,15	13,1 ± 0,1
CaZnOS: Eu^{3+}3%, Tb^{3+}5%	356,22 ± 0,07	43,8 ± 0,1
CaZnOS: Eu^{3+}5%, Tb^{3+}5%	375,61 ± 0,06	40,8 ± 0,1

Table 2 Computed emission average lifetime and emission efficiency

The results, summarized in table 2, clearly show the faster trend of the $^5D_4 \rightarrow {}^7F_5$ transition (540 nm line) of Tb^{3+} ions when co-doping with Europium occurs. This trend seems to be stabilized for Eu^{3+} content close to 3 wt.% evidenced by similar efficiency for higher doping percentage.

The reported results can be summarized in the scheme of the optical levels and transitions depicted in Figure 12. After a proper excitation to the defect levels, a fast and direct energy transfer to the Tb^{3+} levels occur, as evidenced by the decrease in intensity of the matrix defect related luminescence and to the very fast behavior of the broad band at 500 nm. The emissions of Tb^{3+} ions occur from the D_3 levels (giving rise to narrow emission in the 400 - 500 nm spectral range) and more efficiently for high doping concentration, from the D_4 levels for intersystem crossing among the Tb^{3+} ions in the matrix. When the matrix is co-doped with Europium, part of the charge transfers non-radiatively from the D_4 levels of Tb^{3+} to the D levels of Europium. This last passage is more efficient as the Eu^{3+} concentration is higher, as evidenced by the charge transfer efficiency that increases from 13% in the sample with a ratio between Eu^{3+}/Tb^{3+} of 1/5 to about 40% when the ratio increases to 3/5 and 1.

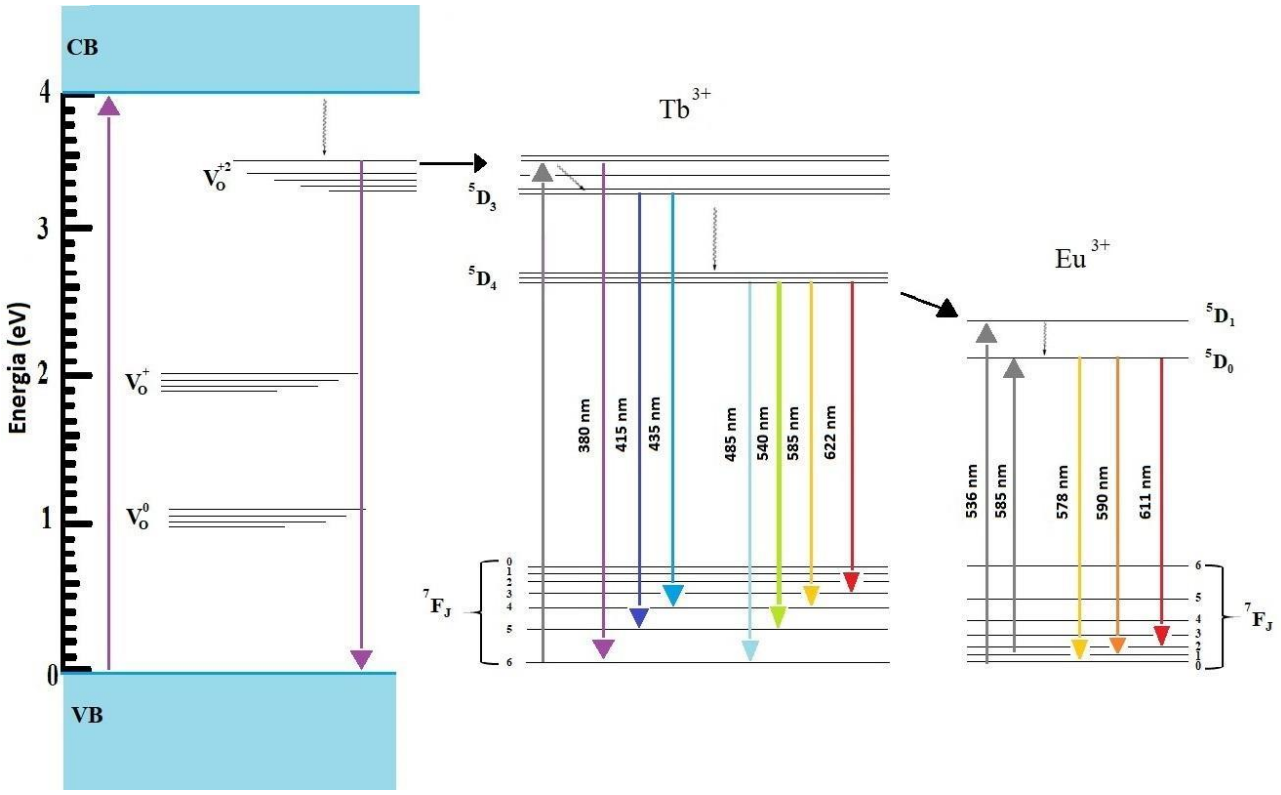

Figure 12. Proposed band model of Tb^{3+}: Eu^{3+}: CaZnOS

It is possible to extend this model to the mechano-luminescence measurements. Du et al., suggest that the excitation form external stimulus generates inner crystal piezo potential with a subsequent tilt of the conduction and valence band [39]. Consequently, the electrons trapped in the defect centers can be released to the conduction band. The recombination kinetics follow, in this case, the same paths of a band-to-band optical excitation. In their model the authors propose that the recombination generates the broad UV band of the matrix or, in the case of RE doping, the energy released is transferred to the excited $^5D_3$ levels of Tb^{3+}, through up conversion process.

The optical properties here reported, strongly suggest a different kinetics in the doped samples, where it is not necessary to recall up-conversion processes, that are very unlikely and with low efficiency, whilst resonance charge transfer from the top of the defect levels to the Tb^{3+} D_3 levels is more likely to occur. The top V_0^{2+} levels are very close to the conduction band, as it was predicted by functional theory computational investigations (0.38 eV [37]) and by experimental observation in pure CaZnOS crystals [25], so a direct transfer to the D_3 levels is not energy forbidden.

As already stated, [40][41], the D_3 levels can easily and efficiently transfer by intersystem energy transfer to D_4 levels of Tb^{3+} ions as well as to the Eu^{3+} centres. These results can be applied to mechano-

luminescence measurements and the relative RE doping can be used to tune the mechano-stimulated emission. Figure 13. reports the CIE coordinates as well as the mechano-luminescence photo, obtained with single impact from a steel ball with radius 0.5 cm and 8.5 g weight at a speed of 4 m/s. As can be observed, a green to red emission can be obtained simply varying the percentage of Tb^{3+} with Eu^{3+}. CIE coordinates spam from red in the Eu^{3+} doped (x=0.5852, y=3921) and heavy doped co-doped sample (x=0.5523, y=0.4091 in Eu^{3+} 5%Tb^{3+}5%) to green (x=0.2495, y=0,4836) in the pure Tb^{3+} sample, with intermedia values in co-doped samples with lower amount of Eu^{3+} (x=0.4398, y=0.4335 for Eu^{3+} 1%Tb^{3+}5% and x=0.5124, y=0,4235 for and Eu^{3+}.

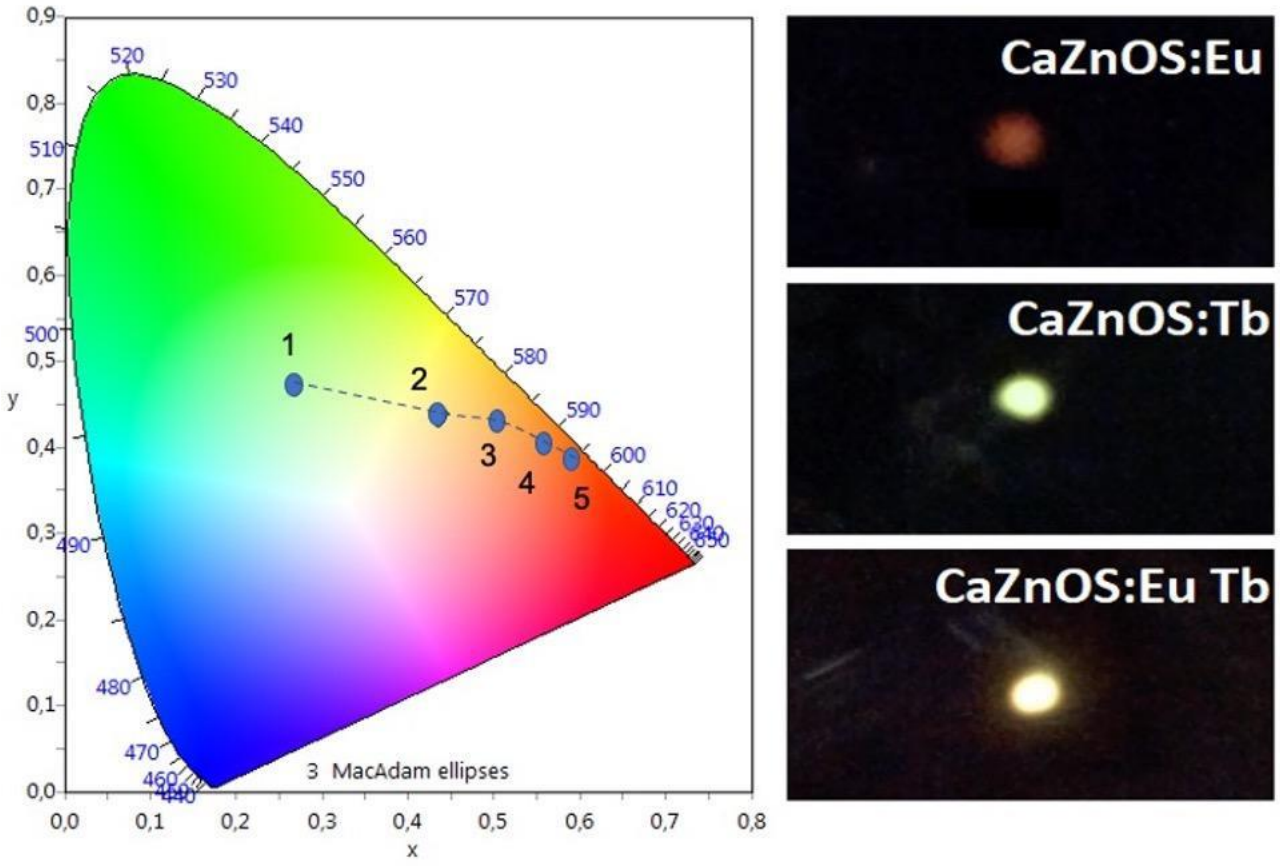

Figure 13. CIE coordinates of luminescence relative to produced samples. Mechano-luminescence. (1) CaZnOS: Tb^{3+}; (2) CaZnOS: Eu^{3+}1%Tb^{3+}5%; (3) CaZnOS: Eu^{3+}3%Tb^{3+}5%; (4) CaZnOS: Eu^{3+} 5%Tb^{3+}5%; (5) CaZnOS: Eu^{3+} 3%Tb^{3+}5%).

2.6. Conclusion

The efficient charge transfer process in CaZnOS doped and co-doped samples has been studied and proven by means of detailed analysis of optical properties.

The experimental and structural characterization (XRD and Raman) as well as DFT calculation on the vibrational properties allows the definition of the preferential doping site for Tb^{3+} and Eu^{3+}. The optical characterizations give more insight in the excitation and emission properties of the doped and co-doped samples. In particular, fast non-radiative channels are activated from the defect centers to Tb^{3+} ions, and the same process was obtained from Tb^{3+} to Eu^{3+}.

Hence, the defect centers can be efficiently utilized as sensitizer for the emission at the rare-earth elements site. Since these defects are responsible of the Mechano-luminescence in CaZnOS system, the model can be shifted from optical excitation to impact excitation.

This work aimed, not only, to define the model of one of the best mechano-luminescent material developed, but also to define the basis for further studies based on the energy transfer mechanism among the dopants centers.

References

[1] Y.C. Lin, M. Karlsson, M. Bettinelli, Inorganic phosphor materials for lighting, Top. Curr. Chem. 374 (2016) 374–421. https://doi.org/10.1007/s41061-016-0023-5.

[2] P.C. Ricci, Assessment of Crystalline Materials for Solid State Lighting Applications: Beyond the Rare Earth Elements, Crystals. 10 (2020) 559. https://doi.org/10.3390/cryst10070559.

[3] L.L. Noto, H.C. Swart, B.M. Mothudi, P.S. Mbule, M.S. Dhlamini, The Dynamics of Luminescence, in: Lumin. - An Outlook Phenom. Their Appl., InTech, 2016. https://doi.org/10.5772/65050.

[4] W. Wu, Y. Duan, B. Liu, Mechanoluminescence: Quantitative Pressure-Brightness Relationship Enables New Applications, Matter. 2 (2020) 291–293. https://doi.org/10.1016/j.matt.2020.01.007.

[5] Y. Zuo, X. Xu, X. Tao, X. Shi, X. Zhou, Z. Gao, X. Sun, H. Peng, A novel information storage and visual expression device based on mechanoluminescence, J. Mater. Chem. C. 7 (2019) 4020–4025. https://doi.org/10.1039/c9tc00641a.

[6] C. Wang, Y. Yu, Y. Yuan, C. Ren, Q. Liao, J. Wang, Z. Chai, Q. Li, Z. Li, HearTb^{3+}eat-Sensing Mechanoluminescent Device Based on a Quantitative Relationship between Pressure and Emissive Intensity, Matter. 2 (2020) 181–193. https://doi.org/10.1016/j.matt.2019.10.002.

[7] S. Krishnan, V. Sundaresan, Mechanoluminescence based structural health monitoring technique for elastomeric components, in: ASME 2016 Conf. Smart Mater. Adapt. Struct. Intell. Syst. SMASIS 2016, American Society of Mechanical Engineers, 2016. https://doi.org/10.1115/SMASIS2016-9054.

[8] J.C.G. Bünzli, K.L. Wong, Lanthanide mechanoluminescence, J. Rare Earths. 36 (2018) 1–41. https://doi.org/10.1016/j.jre.2017.09.005.

[9] Y. Chen, C. Xu, B. Xu, Z. Mao, J.A. Li, Z. Yang, N.R. Peethani, C. Liu, G. Shi, F.L. Gu, Y. Zhang, Z. Chi, Chirality-activated mechanoluminescence from aggregation-induced emission enantiomers with high contrast mechanochromism and force-induced delayed fluorescence, Mater. Chem. Front. 3 (2019) 1800–1806. https://doi.org/10.1039/c9qm00312f.

[10] Y. Xie, Z. Li, The development of mechanoluminescence from organic compounds: Breakthrough and deep insight, Mater. Chem. Front. 4 (2020) 317–331. https://doi.org/10.1039/c9qm00580c.

[11] S.M. Jeong, S. Song, S.K. Lee, N.Y. Ha, Color manipulation of mechanoluminescence from stress-activated composite films, Adv. Mater. 25 (2013) 6194–6200. https://doi.org/10.1002/adma.201301679.

[12] T. Sambrook, C.F. Smura, S.J. Clarke, M.O. Kang, P.S. Halasyamani, Structure and physical properties of the polar oxysulfide CaZnOS, Inorg. Chem. 46 (2007) 2571–2574. https://doi.org/10.1021/ic062120z.

[13]P.C. Ricci, C.M. Carbonaro, A. Casu, C. Cannas, R. Corpino, L. Stagi, A. Anedda, Optical and structural characterization of cerium doped LYSO sol-gel polycrystal films: Potential application as scintillator panel for X-ray imaging, J. Mater. Chem. 21 (2011) 7771–7776. https://doi.org/10.1039/c1jm10492f.

[14] M. Nazarov, D.Y. Noh, New generation of Eu3+ropium- and Terbium-activated phosphors: From syntheses to applications, 2011. https://doi.org/10.4032/9789814364058.

[15] Y.L. Yang, Y. Zhou, D.J. Pan, Z.J. Zhang, J.T. Zhao, The luminescence properties of CaZnOS: Bi3+, Sm3+, Li+ phosphors with tunable emissions and energy transfer for white emission, J. Lumin. 206 (2019) 578–584. https://doi.org/10.1016/j.jlumin.2018.10.046.

[16] Z. Qiu, C. Rong, W. Zhou, J. Zhang, C. Li, L. Yu, S. Liu, S. Lian, A strategy for synthesizing CaZnOS: Eu3+2+ phosphor and comparison of optical properties with CaS:Eu3+2+, J. Alloys Compd. 583 (2014) 335–339. https://doi.org/10.1016/j.jallcom.2013.08.162.

[17] Z. Xu, Z. Xia, B. Lei, Q. Liu, Full color control and white emission from CaZnOS: Ce3+,Na+,Mn2+ phosphors: Via energy transfer, J. Mater. Chem. C. 4 (2016) 9711–9716. https://doi.org/10.1039/c6tc03016e.

[18] R. Ma, S. Mao, C. Wang, Y. Shao, Z. Wang, Y. Wang, S. Qu, D. Peng, Luminescence in Manganese (II)-Doped SrZn2S2O Crystals from Multiple Energy Conversion, Front. Chem. 8 (2020) 752. https://doi.org/10.3389/fchem.2020.00752.

[19] Z.J. Zhang, A. Feng, X.Y. Chen, J.T. Zhao, Photoluminescence properties and energy levels of RE (RE = Pr, Sm, Er, Tm) in layered-CaZnOS oxysulfide, J. Appl. Phys. 114 (2013) 213518. https://doi.org/10.1063/1.4842815.

[20] L. Stagi, D. Chiriu, A. Ardu, C. Cannas, C.M. Carbonaro, P.C. Ricci, Luminescence enhancement by energy transfer in melamine-Y2O3:Tb^{3+} nanohybrids, J. Appl. Phys. 118 (2015) 125502. https://doi.org/10.1063/1.4931678.

[21] L. Lin, T. Wanjun, Effects of Tb^{3+} doping on luminescence properties of NaMg4(PO4)3:Eu3+2+, J. Lumin. 198 (2018) 405–409. https://doi.org/10.1016/j.jlumin.2018.03.001.

[22] X. Zhang, L. Zhou, Q. Pang, J. Shi, M. Gong, Tunable luminescence and Ce3+ → Tb^{3+} → Eu3+3+ energy transfer of broadband-excited and narrow line red emitting Y2SiO5:Ce3+, Tb^{3+}, Eu^{3+} phosphor, J. Phys. Chem. C. 118 (2014) 7591–7598. https://doi.org/10.1021/jp412702g.

[23] Z. Qiu, H. Lian, T. Luo, J. Fan, X. Cai, Z. Cheng, M. Shang, S. Lian, J. Lin, One-step structure-directing approach to Ce3+-doped CaS luminescent micro-nanocrystals, CrystEngComm. 17 (2015) 8676–8682. https://doi.org/10.1039/c5ce01800e.

[24] B. Budde, H. Luo, P. Dorenbos, E. van der Kolk, Luminescent properties and energy level structure of CaZnOS: Eu3+2+, Opt. Mater. (Amst). 69 (2017) 378–381. https://doi.org/10.1016/j.optmat.2017.04.045.

[25] P.C. Ricci, J. Satta, D. Chiriu, R. Corpino, C.M. Carbonaro, M. Salis, C. Melis, P.S. Normile, J.A. De Toro, Optical and vibrational properties of CaZnOS: The role of intrinsic defects, J. Alloys Compd.

777 (2019) 225–233. https://doi.org/10.1016/j.jallcom.2018.10.311.

[26] Z. Xu, Z. Xia, Q. Liu, Two-Step Synthesis and Surface Modification of CaZnOS: Mn^{2+} Phosphors and the Fabrication of a Luminescent Poly(dimethylsiloxane) Film, Inorg. Chem. 57 (2018) 1670–1675. https://doi.org/10.1021/acs.inorgchem.7b03060.

[27] J.J. Joos, K. Lejaeghere, K. Korthout, A. Feng, D. Poelman, P.F. Smet, Charge transfera induced energy storage in CaZnOS: Mn - Insight from experimental and computational spectroscopy, Phys. Chem. Chem. Phys. 19 (2017) 9075–9085. https://doi.org/10.1039/c7cp00285h.

[28] P. Han, X. Jiang, L. Zhang, F. Yu, Q. Shi, Y. Ding, Q. Zhang, Effect of Li2CO3 flux on the preparation temperature, particle micro morphology and light absorption performance of samarium borate by solid state method, J. Mater. Sci. Mater. Electron. 26 (2014) 666–670. https://doi.org/10.1007/s10854-014-2447-4.

[29] P. Han, X. Jiang, L. Zhang, F. Yu, Q. Shi, Y. Ding, Q. Zhang, Effect of Li2CO3 flux on the preparation temperature, particle micro morphology and light absorption performance of samarium borate by solid state method, J. Mater. Sci. Mater. Electron. 26 (2014) 666–670. https://doi.org/10.1007/s10854-014-2447-4.

[30] P. Giannozzi, S. Baroni, N. Bonini, M. Calandra, R. Car, C. Cavazzoni, D. Ceresoli, G.L. Chiarotti, M. Cococcioni, I. Dabo, A. Dal Corso, S. De Gironcoli, S. Fabris, G. Fratesi, R. Gebauer, U. Gerstmann, C. Gougoussis, A. Kokalj, M. Lazzeri, L. Martin-Samos, N. Marzari, F. Mauri, R. Mazzarello, S. Paolini, A. Pasquarello, L. Paulatto, C. Sbraccia, S. Scandolo, G. Sclauzero, A.P. Seitsonen, A. Smogunov, P. Umari, R.M. Wentzcovitch, QUANTUM ESPRESSO: A modular and open-source software project for quantum simulations of materials, J. Phys. Condens. Matter. 21 (2009). https://doi.org/10.1088/0953-8984/21/39/395502.

[31] J.P. Perdew, K. Burke, M. Ernzerhof, Generalized Gradient Approximation Made Simple [Phys. Rev. Lett. 77, 3865 (1996)], Phys. Rev. Lett. 78 (1997) 1396–1396. https://doi.org/10.1103/PhysRevLett.78.1396.

[32] D. Vanderbilt, Soft self-consistent psEu3+dopotentials in a generalized eigenvalue formalism, Phys. Rev. B. 41 (1990) 7892–7895. https://doi.org/10.1103/PhysRevB.41.7892.

[33] P. Giannozzi, S. de Gironcoli, P. Pavone, S. Baroni, Ab initio calculation of phonon dispersions in semiconductors, Phys. Rev. B. 43 (1991) 7231–7242. https://doi.org/10.1103/PhysRevB.43.7231.

[34] L. Lutterotti, Total pattern fitting for the combined size-strain-stress-texture determination in thin film diffraction, Nucl. Instruments Methods Phys. Res. Sect. B Beam Interact. with Mater. Atoms. 268 (2010) 334–340. https://doi.org/10.1016/j.nimb.2009.09.053.

[35] T. Sambrook, C.F. Smura, S.J. Clarke, M.O. Kang, P.S. Halasyamani, Structure and physical properties of the polar oxysulfide CaZnOS, Inorg. Chem. 46 (2007) 2571–2574. https://doi.org/10.1021/ic062120z.

[36] C.J. Duan, A.C.A. Delsing, H.T. Hintzen, Photoluminescence properties of novel red-emitting Mn2+- activated MZnOS (M = Ca, Ba) phosphors, Chem. Mater. 21 (2009) 1010–1016. https://doi.org/10.1021/cm801990r.

[37] C. Pan, J.C. Zhang, M. Zhang, X. Yan, Y.Z. Long, X. Wang, Intrinsic oxygen vacancies mediated multi-mechano-responsive piezoluminescence in undoped zinc calcium oxysulfide, Appl. Phys. Lett. 110 (2017) 1–6. https://doi.org/10.1063/1.4985012.

[38] J.R. Lakowitz, Energy Transfer, in: Princ. Fluoresc. Spectrosc., Springer US, 2006: pp. 443–475. https://doi.org/10.1007/978-0-387-46312-4_13.

[39] Y. Du, Y. Jiang, T. Sun, J. Zhao, B. Huang, D. Peng, F. Wang, Mechanically Excited Multicolor Luminescence in Lanthanide Ions, Adv. Mater. 31 (2019) 1–8. https://doi.org/10.1002/adma.201807062.

[40] M. Back, R. Marin, M. Franceschin, N. Sfar Hancha, F. Enrichi, E. Trave, S. Polizzi, Energy transfer in color-tunable water-dispersible Tb^{3+}-Eu^{3+} codoped CaF2 nanocrystals, J. Mater. Chem. C. 4 (2016) 1906–1913. https://doi.org/10.1039/c5tc03355a.

[41] P.C. Ricci, C.M. Carbonaro, R. Corpino, C. Cannas, M. Salis, Optical and structural characterization of terbium-doped Y 2SiO5 phosphor particles, J. Phys. Chem. C. 115 (2011) 16630–16636. https://doi.org/10.1021/jp203523s.

Optimizing Mechano-Luminescent Properties of CaZnOS: Tb via Microwave-Assisted Synthesis: A Comparative Study with Conventional Thermal Methods.

Ugbo Franca Chika[a], Stefania Porcu[a], Riccardo Corpino[a], Andrea Pinna[a], Carlo Maria Carbonaro[a], Daniele Chiriu[a], Smet Philippe F.[b], Pier Carlo Ricci[a*]

Materials 2023, 16, 3511. https://doi.org/10.3390/ma16093511

3.1. Abstract:

Recent developments in lighting and display technologies have led to an increased focus on materials and phosphors with high efficiency, chemical stability, and eco-friendliness. Mechano-luminescence (ML) is a promising technology for new lighting devices, specifically in pressure sensors and displays. CaZnOS has been identified as an efficient ML material, with potential applications as a stress sensor.

This study focuses on optimizing the mechano-luminescent properties of CaZnOS: Tb through microwave-assisted synthesis. We successfully synthesized CaZnOS doped with Tb^{3+} using this method and compared it with samples obtained through conventional solid-state methods. We analysed the material's characteristics using various techniques to investigate their structural, morphological, and optical properties. We then studied the material's mechanoluminescent properties through single impacts with varying energies. Our results show that materials synthesized through microwave methods exhibit similar optical and, primarily, mechano-luminescent properties, making them suitable for use in photonics applications. The comparison of the microwave and conventional solid-state synthesis methods highlights the potential of microwave-assisted methods to optimize the properties of mechano-luminescent materials for practical applications.

3.2. Introduction

Nowadays there is an extensive demand for innovative materials and techniques that allow to reduce energy consumption and guarantee the sustainable development in different fields, like wind turbines, solar panels, electric beams, energy-efficient lighting (LEDs), consumer electronics, durable metals, automotive, aerospace, and medical equipment.

In the field of chemistry, the use of mechanical energy has been already widely utilized for providing a solution-free, energy saving, high-productivity, and low-temperature process [1][2][3]. In the field of

phosphors and sensors, the mechanoluminescent effect is increasing its importance thanks to the development of intriguing new materials [4][5]. Inner crack visualization, biological stress, light source, and ultrasonic powder recording are just few already developed fields of application [6][7][8]. Mechanoluminescent materials can be activated not only through impacts, but also through sound waves, loads and, indirectly, through the application of external magnetic fields [9][10][11][12].

A key element was the development of materials with high efficiency in the transformation of the mechanical stress in optical emission. Among these, a specific place is held by CaZnOS whose mechanoluminescent properties were published for the first time only in 2013 and the first structural characterizations just 8 years earlier [13]. CaZnOS, doped (and co-doped) with rare-earth elements such as Eu, Tb, Er, Pr, Sm, Er, Tm or with transition metals (Cu, Al, Mn) is highly efficient both as a phosphor and as a mechanoluminescent material depending on the structural defects of the matrix and how the emitter element interacts with the defects themselves [14][15][16][17][18][19][20]. The structure can be easily doped with rare earth elements for their similar ionic radius of Ca, and, among the other Tb represents one of the popular dopants of high green-luminescence from its $^5D_4 \rightarrow {}^7F_J$ transition (where J = 3, 4, 5, 6), with recombination time spanning from microseconds to milliseconds (μs-ms). Further, Tb^{3+} is usually co-doped with other rare earth elements in different host matrix, acting both as sensitizer or activator [15][21][22].

In CaZnOS structure, the shallow traps connected to Ca vacancies are responsible for the high mechano-luminescence effects as well for the persistent luminescence. When a mechanical load is applied, a local piezoelectric field is produced causing band bending and triggering the release of trapped charges to the recombination sites (i.e., the dopants) [23].

Therefore, defects play a crucial role to obtain a well-defined crystalline structure, which can be achieved through easily reproducible synthesis processes. The traditional method for obtaining CaZnOS involves a solid-state synthesis process that is conducted at high temperatures between 1050 and 1200 °C for a period of 4-8 hours. This method is known for its excellent reproducibility of the resulting materials, but it is also energy intensive. The heating process is slow and complex, requiring a long processing time to convert the materials into useful products. Additionally, the thermal energy transfer from the source is often inefficient, as it must pass through the walls of the container before reaching the substance inside, leading to insufficient heating of the material.

To overcome the time-consuming process and achieve a material with highly efficient luminescence, researchers and scientists are exploring the use of microwave technology for synthesizing phosphor materials. [24][25]

The use of microwave (MW) methods for the synthesis of materials offers several advantages compared to other methods such as sol-gel, solid-state, combustion-assisted, and hydrothermal synthesis. One of the main advantages of MW methods is the drastic reduction in synthesis time, making it a fast and efficient method. Additionally, the equipment required for MW synthesis is relatively simple and easy to use, requiring no specialized knowledge or skills to operate. This also makes it a cost-effective method as it does not require expensive equipment or specialized facilities.

MW methods have been found to produce high-quality materials with high yield, making them ideal for industrial applications. Additionally, the materials produced using MW methods are eco-friendly as they consume less energy and produce less waste than traditional methods.[24] The powder materials produced by MW methods are also suitable for industrial applications without the need for annealing to improve their optical properties. Overall, MW methods offer a flexible and cost-effective method for the synthesis of new materials in the form of crystals or liquids, with improved properties that are readily applicable for industrial use.

The rapid and uniform heating of the reaction mixture is attributed to the dielectric properties of the materials, which enable the absorption of microwave energy and subsequent conversion into heat. The interaction between microwaves and the reaction mixture is dependent on the frequency of the radiation, the dielectric properties of the materials, and the geometry of the reaction vessel. As the microwaves penetrate the reaction mixture, they induce rotational and vibrational motion of the molecules, leading to a rapid increase in temperature. The localized and rapid heating of the reaction mixture can facilitate the formation of the desired products, resulting in shorter reaction times and higher yields. This is due to the rapid and localized heating of the reaction mixture, which can lead to the formation of nucleation sites and the subsequent growth of crystals in a controlled manner.

Overall, the use of microwave-assisted synthesis offers several advantages over conventional methods, including shorter reaction times, higher yields, and the formation of unique crystal structures and morphologies.

As sketched in the scheme of Figure 14, microwave irradiation generates heat within the material and throughout its entire mass simultaneously, as this excitation process results in a consistent and uniform heating of the material, leading to a rapid and homogenous increase in temperature.

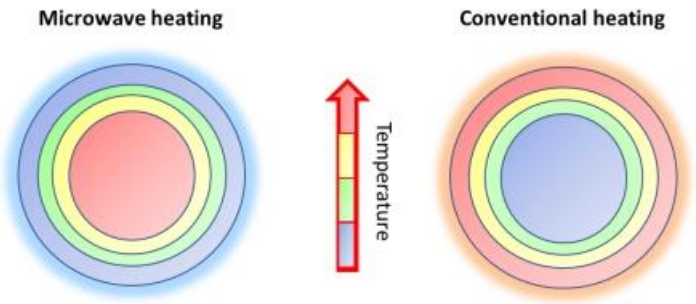

Figure 14. Schematic representation of Microwave heating vs Conventional heating

Often the use of MW techniques is assisted by a thermal effect with the scope to start the real MW reaction (generating an intermediate compound) or to assist the synthesis by increasing the ion mobility. [2]

MAS (Microwave Assisted Synthesis) is a relatively new method for the synthesis of a wide range of materials, including both pure and doped organic, inorganic, metallic, ceramics, polymers, composites, and sulfide phosphors. It is a fast and efficient method that can significantly reduce the synthesis time compared to traditional methods. The technique is based on the use of microwave energy to heat and excite the molecules of the material being synthesized, leading to a rapid and homogenous increase in temperature and has many advantages over traditional synthesis methods, including:

- Reduced synthesis time
- Consistent and uniform heating of the material
- High-quality materials with high yield
- Eco-friendly, as it consumes less energy and produces less waste than traditional methods.
- Cost-effective, as it requires less equipment and facilities than traditional methods.

Furthermore, it is a versatile technique that can be used to synthesize a wide range of materials with improved properties and are readily applicable for industrial use.[26][27]

MASS has proven to be a practical method for synthesizing both pure and doped organic, inorganic, metallic, ceramics, polymers, composites, and sulfide phosphors [14, 15], such as Y_2O_3:Eu^{3+} [28] $CaCO_3$:Eu^{3+} [29]; $CaGd_2(WO_4)_4$: Er^{3+}/Yb^{3+}[30] and, Gd_2O_2S: Tb^{3+}[31].

It is worth noting that several studies have demonstrated the effectiveness of MAS in synthesizing various inorganic phosphor materials, with excellent results. For example, Carvalho et al. [32] successfully used microwave methods to synthesize high-quality persistent luminescence materials, such as

$Sr_2MgSi_2O_7:Eu^{2+}$, Dy^{3+}. In another study conducted by Jiawei Bi et al. [28], Eu^{3+} doped Y_2O_3 nanophosphors were synthesized using a simple, ultra-fast, and environmentally friendly method combining ultrasonic and microwave techniques, obtaining a material with excellent optical properties.
In the present study, samples of CaZnOS doped with Tb were synthesized using MAS technique, with synthesis times of 10, 20, and 30 minutes. The samples were characterized using a multi-technique approach with particular attention to the mechanoluminescence properties. Afterwards, the structural, morphological, and optical properties were compared to those of the sample obtained via solid state synthesis.
The results of this study demonstrated that the microwave-assisted synthesis method is a valid and cost-effective method for the synthesis of phosphors with enhanced mechanoluminescence efficiency when compared to the sample obtained using solid-state synthesis. Overall, this study highlights the potential of microwave-assisted synthesis as a promising method to produce efficient and cost-effective oxysulfide phosphors.

3.3. **Experimental**

3.3.1. Materials and Methods

Terbium doped CaZnOS samples (wt. 5%) were prepared by MASS method starting from $CaCO_3$, ZnS, Tb_4O_7 and Li_2CO_3 powders:

$$(1\text{-}0.05)\ CaCO_3 + ZnS + 0.0125Tb_4O_7 \rightarrow Ca_{(0.95)}\ ZnOSTb_{0.05} + CO_2 \qquad (6)$$

Due to the similar ionic radius (99pm for Ca^{2+}, 74pm for Zn^{2+} 4-coordinate and 95pm for Tb^{3+} in 6-coordination), Tb^{3+} ions substitute Ca^{2+} ions. However, considering the larger charge states than Ca^{2+}, Li_2CO_3 was necessary for charge balance purposes and as reaction catalyst. It was added in excess with respect the stoichiometry amounts both in the solid-state and microwave-assisted synthesis. To obtain about 0.8 g of Tb doped CaZnOS the following amounts were utilized: 0,4795 g di CaCO3, 0,4870g, ZnS and 0,0045g Tb_4O_7.

3.3.2 MAS synthesis: The mixture was transferred to a small crucible (10 ml), which was placed within a larger crucible containing activated charcoal. The larger crucible was covered with a lid and placed in

the microwave with a power of 750W. The samples were microwaved for 10, 20, and 30 minutes, respectively, and then left to cool down naturally in the air (hereafter referred as MW10min, MW20min, and MW30min, respectively). Figure 15 reports the photographs of the sample during the synthesis (the thermal effect is clearly visible) and after it was cooled down to room temperature. It is worth to note that a thin carbon layer is deposited on the top surface of the sample. This layer has been removed from the samples with the aid of a clean spatula before the study, even if a small percentage of carbon cannot be totally excluded. Additional samples were prepared without the use of activated charcoal to investigate the effect of the charcoal as an additional heat absorber on the synthesized materials.

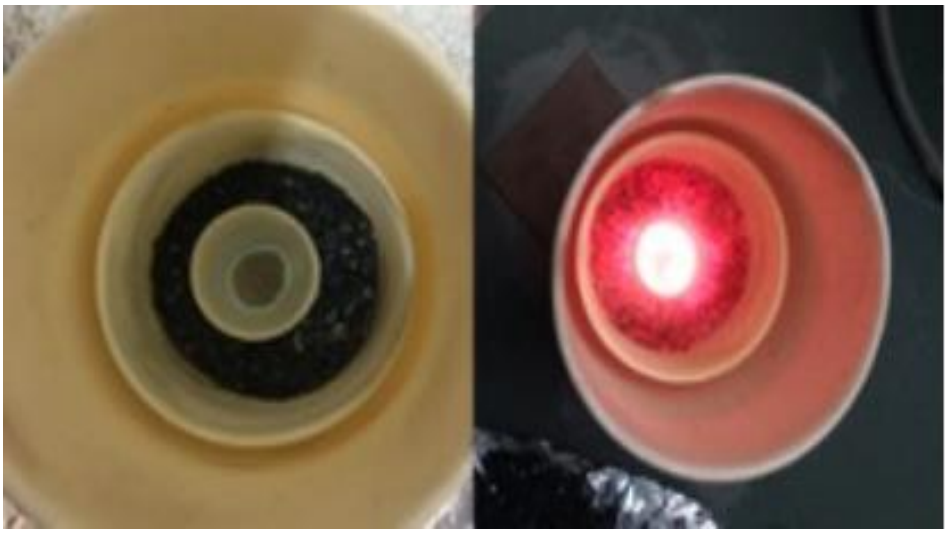

Figure 15. View of the Microwave assisted synthesis (MAS), on the left: the sample after the synthesis, on the right, during the synthesis.

3.3.3. Solid state (SS) synthesis: The precursor mixture was placed in an alumina crucible (10 ml) and then sintered in a tubular furnace under a constant flow of nitrogen gas. The temperature was gradually increased to 1000 °C at a ramp rate of 10 °C/min and held at that temperature for 5 hours. After that, the samples were allowed to cool down naturally to room temperature (here after named SS sample).

3.4. Characterization techniques

The powders were characterized using X-ray diffraction, PL, Raman, Mechanoluminescence, and Time-resolved Luminescence to check the structural, optical, and ML properties.

Raman spectroscopy measurements were performed using an MS750 spectrograph (Sol-Instruments) equipped with a 600 gr/mm grating. A 785 nm laser was used as the excitation source, focused through a 10X Olympus objective lens with an estimated laser power of $7.5x10^3$ W/cm^2. No heating effect on the samples has been revealed. The measurements were conducted at room temperature, with a spectral resolution of 1 cm^{-1}.

X-ray diffraction measurements were conducted using a Bruker D8 Advance diffractometer operating at 30 kV and 20 mA. The diffractometer was equipped with a Cu tube as the X-ray source (wavelength of 1.5418 Å) and a Vantec-1 PSD detector. The powder patterns were collected in the 2θ range of 10° to 70°.

Steady-state photoluminescence measurements were conducted using a filtered light from a laser-driven Xenon lamp (EQ-99X) that had a final bandwidth of approximately 1 nm. The emitted photoluminescence was collected using an optical fiber and directed to an Avantes Thermo-Electric Cooled spectrometer for analysis.

Time-resolved luminescence measurements were performed using an optical parametric oscillator with a frequency doubler device, which was pumped by the third harmonic (355 nm) of a pulsed Nd:YAG laser (Quanta Ray Pro 730). The excitation pulse width at half-maximum was 8 ns with a repetition rate of 10 Hz, and a spectral bandwidth less than 0.3 cm^{-1}. The collected signal was dispersed by a spectrograph (Arc-SpectraPro 300i) with a spectral bandpass of less than 2.5 nm and detected by a gateable intensified CCD (PI MAX Princeton Inst.). To minimize the dark current, the detector was cooled to -20°C using a Peltier device.

3.3.4.Mechanoluminescent Test

The mechanical pulse for the mechano-emission was generated by dropping a stainless-steel ball (10 mm diameter, 8.15 g) from a height of about 1 meter onto layers of powder approximately 0.5 mm thick. The impact speed was measured to be 4 m/s using an Airsoft E9800-X anemometer. The impact zone was placed on a transparent CaF_2 substrate, and the emitted light was collected from the opposite side and focused onto an intensified CCD (PI MAX Princeton Inst.).

3.4 Results and Discussion

Structural characterization plays a crucial role in this study, as it provides insight into the crystal structure and phase purity of the samples. Figure 16 displays the X-ray diffraction patterns of samples synthesized using the MAS approach at different time intervals. Additionally, for comparison, the XRD pattern of the sample obtained through the SS reaction method is also included in the figure to provide a clear comparison of the structural properties of the samples synthesized using the different techniques.

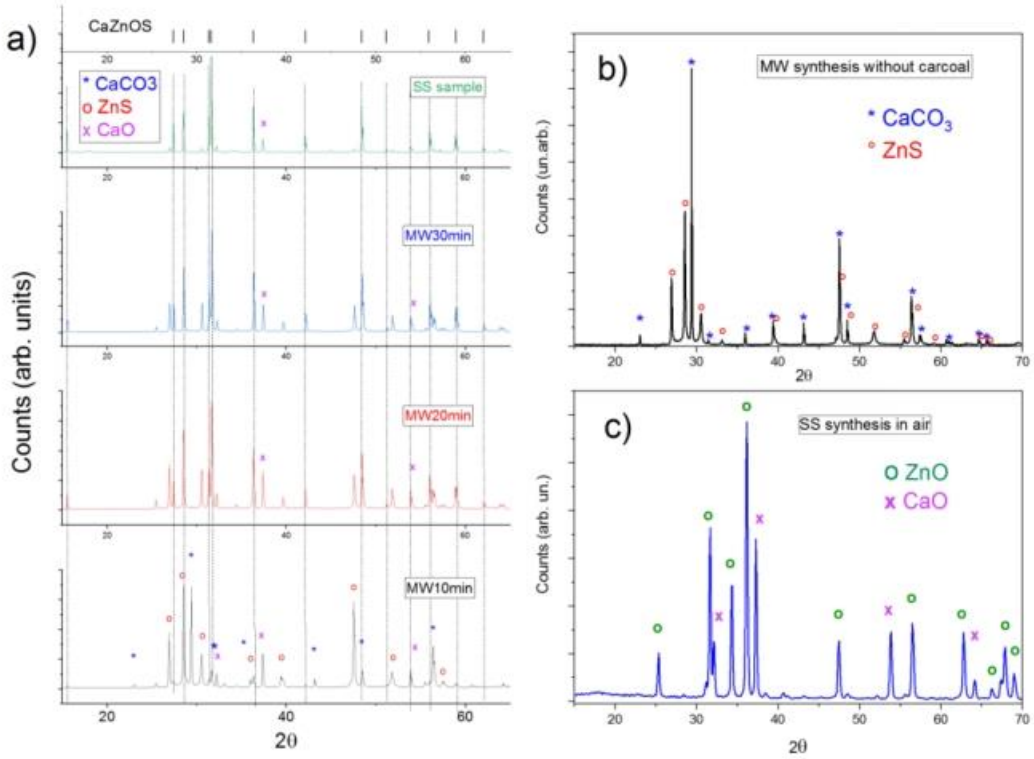

Figure 16. a) X-Ray diffraction patterns of SS and MW synthesized Tb doped CaZnOS samples. The vertical dashed lines indicate the diffraction angles for CaZnOS. The main diffraction lines for impurity phases are indicated as well. b) X-Ray diffraction pattern of microwave synthetized sample in absence of Charcoal, c) X-Ray diffraction pattern of solid-state sample growth in air.

The SS sample pattern, analysed by means of the software MAUD for multi pattern fitting [33], reveals the presence of CaZnOS (Reference ICSD card no. 245309) with a percentage of 90% and residuals of ZnS and CaO in low percentage.

In the XRD patterns of the MAS samples, the presence of the starting precursors is clearly visible. As expected, the sample obtained at the shortest irradiation time has a higher content of unreacted precursors, which decreases with the duration of microwave treatment. The CaZnOS phase is observed to increase from around 35% after 10 minutes, with a high percentage of precursors $CaCO_3$, CaO and ZnS, to 60% at 20 minutes, where residuals of CaO and ZnS are also present in moderate percentages. Further increases in the synthesis time do not result in a significant increase in the weight percentage of CaZnOS, nor in the formation of any other competitive reactions.

The presence of CaO can be strictly related to the chamber atmosphere. It was already observed that a reducing atmosphere is strictly required for the formation of CaZnOS, while the growth in air generates only oxides. In the MAS process, the reducing atmosphere is provided by the high percentage of CO_2 generated by the thermal effect of the charcoal present in the outer crucible [20]. In absence of charcoal, the CaZnOS structure was not formed, both for the presence of a not reducing atmosphere (in the SS synthesis in air, only CaO and ZnS are formed), but also for the lower temperature of the starting precursor (Figure 16b and 16c).

The Raman spectrum of the SS-CaZnOS sample displays all the characteristic bands expected in the CaZnOS structure (Figure 17a). with the most prominent ones at 75 cm^{-1}, 102 cm^{-1}, 124 cm^{-1}, and 272 cm^{-1}. [20]

These peaks correspond to the double degenerate vibration E modes, specifically the anti-symmetric E_2 mode and the symmetric E_1 mode. The region at lower wavenumbers (50 cm^{-1}–150 cm^{-1}) is sensitive to the vibrations of heavier elements and can provide information about the presence of rare earth dopant elements in the sample. [15]

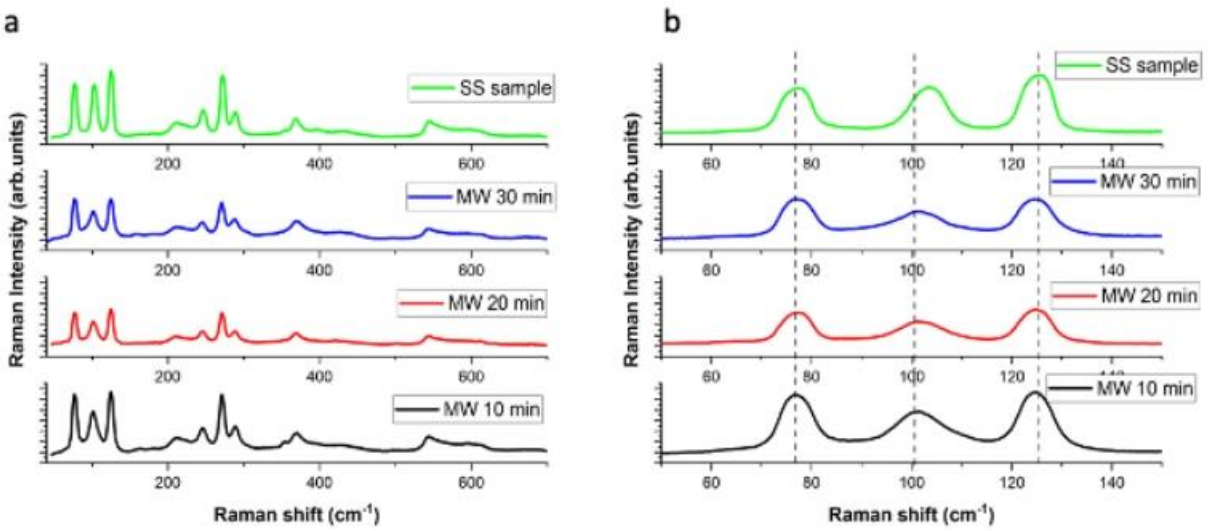

Figure 17. Raman spectra of SS and MW synthesized Tb doped CaZnOS samples

The findings from the Raman measurements are consistent with the results obtained from the X-ray diffraction analysis. The Raman spectrum of the MW10min sample displays the main characteristics of the CaZnOS matrix, however, an additional peak at 348 cm^{-1} is also observed, providing evidence of the presence of ZnS in the sample.

However, a general comparison of the Raman spectra shows a similar behavior across all samples, with the main variations being observed only in the low-energy region (50-150 cm^{-1}).

Three main bands are clearly visible in the Raman spectra of the samples (Figure 17b), corresponding to the two E2 modes at 75 and 102 cm^{-1} and the E1 mode at 125 cm^{-1}. It is noteworthy that these bands remain centered at the same Raman frequency and show no significant variations in their width, as can be seen when comparing the spectra of the samples grown by MAS and the SS synthesis method.

On the contrary, a clear variation can be observed in the central E2 band at 102 cm^{-1}, both in position (the band is peaked at 100 cm^{-1} in the MW samples) and band width. This band is primarily associated with the vibrations of the Ca ions in the lattice, while the other two modes are primarily related to the vibrations of the Zn ions in the lattice.[15]

The presence of impurity phases (such as CaO) in the samples may introduce lattice defects associated with Ca, and O vacancies in the CaZnOS matrix. These defects can result in a broadening and shifting of the Raman bands due to the altered short-range order near the Ca vacancies.

The elemental distribution obtained from EDAX measurements can give important indication and proof of local inhomogeneities. Even if the CaZnOS structure is the predominant phase, a deep analysis permits

to find some aggregates of different structures. The Figure 18 shows the presence of inhomogeneous zones with clusters of Ca and S (most probable CaS, white circle) and Zn, S (ZnS, red circle). However, the presence of CaS was relatively low (under the detection limit of the XRD results) and the inhomogeneities are restricted to a limited number of zones.

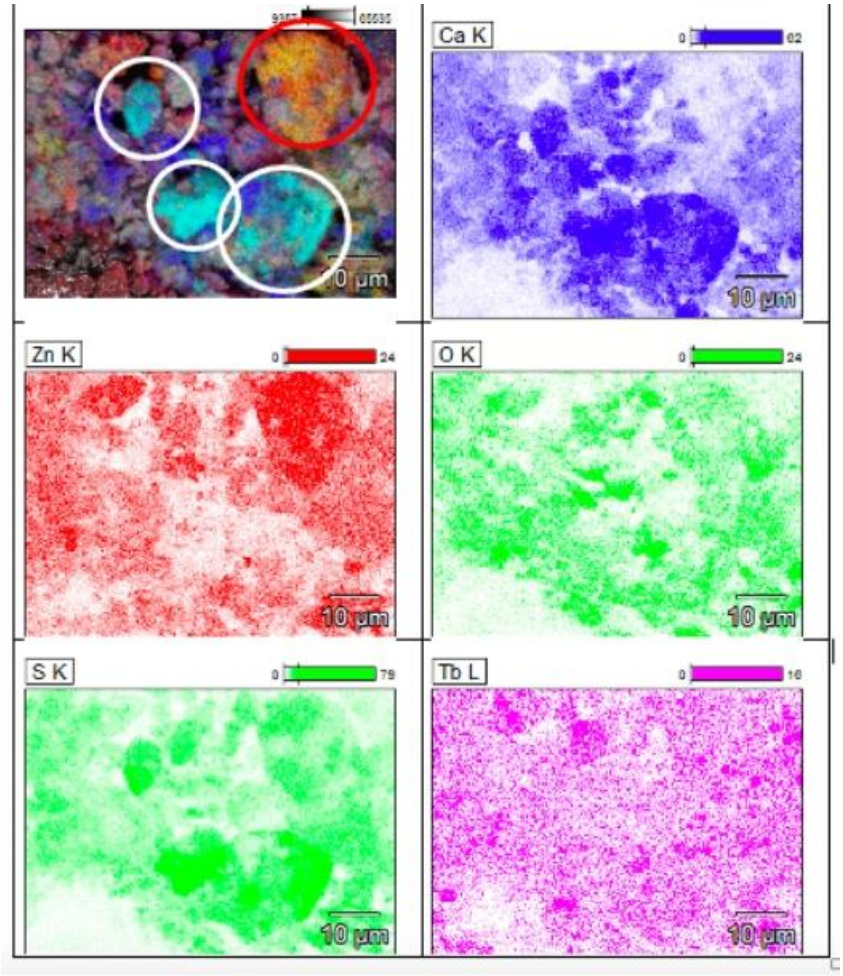

Figure 18. Results of EDAX analysis of the MW20min sample. The white and red circles indicate the presence of clusters of Calcium and Zinc, respectively.

The optical properties confirm the similarity between the sample obtained by solid state synthesis and the MAS growth sample (MW20min).

The main features of the photoluminescence spectra come from the recombination at the Tb sites, where the narrow emissions below 500 nm are related to the transitions from the $^5D_3$ excited levels to the ^7F_J ground states of the rare earth, while the main features in the 490-600 nm spectral region are due to the recombination from the $^5D_4$ levels [34].

The excitation spectrum of the SS sample present direct excitation channel in the deep UV region (240-280 nm), related to band-to-band excitation of the matrix and direct excitation of the Tb levels.

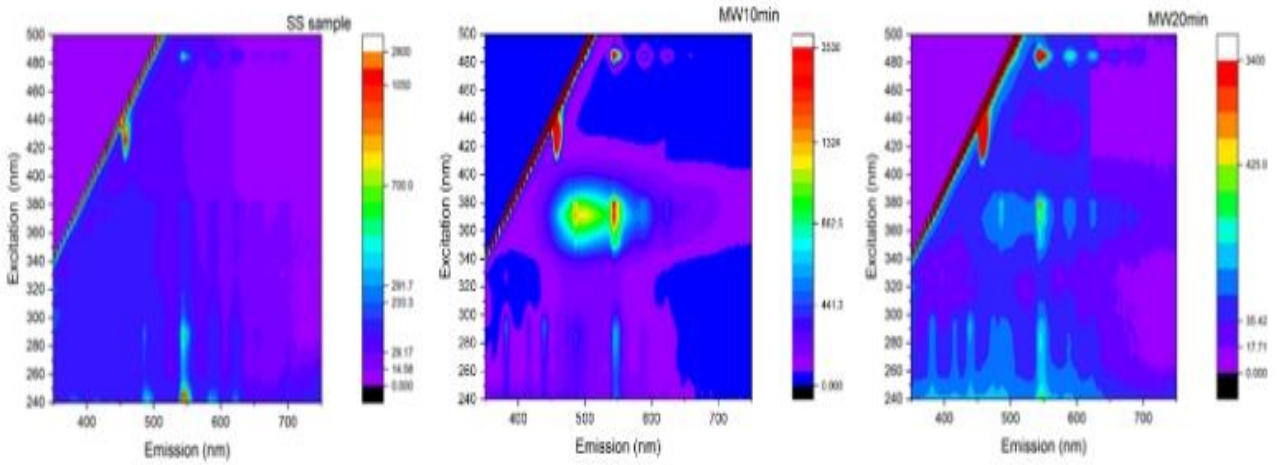

Figure 19 3D plot of the excitation and emission spectra for SS samples, MW10min and MW20min samples

The MAS sample at 10 minutes presents a broad emission band centered at about 500 nm with excitation between 340 and 400 nm. Upon increasing the duration of the microwave treatment this band decreases its importance. As it was already indicated in previous works [20] [35][36], the latter band is due to the presence of oxygen vacancies, VO^{2+}, generated as consequences of Ca and S vacancies and can be efficiently utilized as sensitizer for the emission at the rare-earth elements site. Further and dedicated measurements should be addressed to fully confirm this assignment.

Time-resolved measurements provide a deeper understanding of the different distributions in the samples obtained through SS and MAS methods. (Figure20).

In the SS-sample, the decay from the $^5D_4 \rightarrow {}^7F_5$ level is monitored at 545 nm with excitation at 280 nm and follows a single exponential behavior with time constant of about 900 microseconds. This value suggests the presence, of non-radiative recombination pathways [34]. Further, the single exponential behavior suggests that the decay is dominated by only one type of recombination path in the SS-sample.

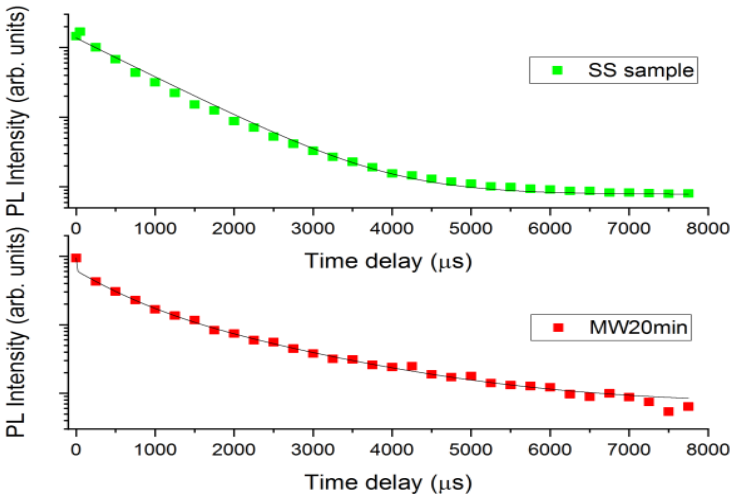

Figure 20. Time decay behaviour of SS and MW20min samples.

On the other hand, the recombination in the MW sample exhibits a more complex behaviour due to the presence of various non-radiative recombination pathways. It is possible to use the following equation to obtain a quantitative value and determine an average lifetime: [37]

$$\tau = \frac{\int_0^T I(t) \cdot t\mathrm{d}t}{\int_0^T I(t)\mathrm{d}t} \qquad (7)$$

Where I(t) is the time-dependent photoluminescence intensity and T is the duration of the time window (8 ms in our case) or can be considered infinite in a more general case. The value of the average lifetime for the samples MW20min and MW30min is 769μs and 750 μs, respectively.

Both the SS and MW20 samples exhibit strong mechanoluminescent properties, as evidenced by the intense light emitted during the mechanical pulse (Figure 21c). The green colour of the emission confirms that the emitting centers are Tb ions, as further confirmed by the spectral dependence (inset in figure 21a).

To deeper define the behaviour of the mechanoluminescent properties of the samples, the single impact effect has been studied. The samples were hit with a stainless-steel ball at different speeds, and the

emitted light was collected through a CaF_2 substrate. The powder layer of the samples, about 0.5 mm thick, was placed on the substrate to measure the light emitted upon impact. However, it is important to note that not all the kinetic energy from the ball is transferred to the powder, as the ball also rebounds. This means that only a fraction of the impact energy is transferred to the samples.

From the height reached from the ball after the impact, it is possible to estimate the energy not transferred to the sample during the impact (about 20% for all the impacts). The inset in Figure 8a reports the spectral shape of the light emitted and the overall intensity from the peak at 545 nm of the Tb emission. The data reported in the main panel is the result of the average of 5 impacts.

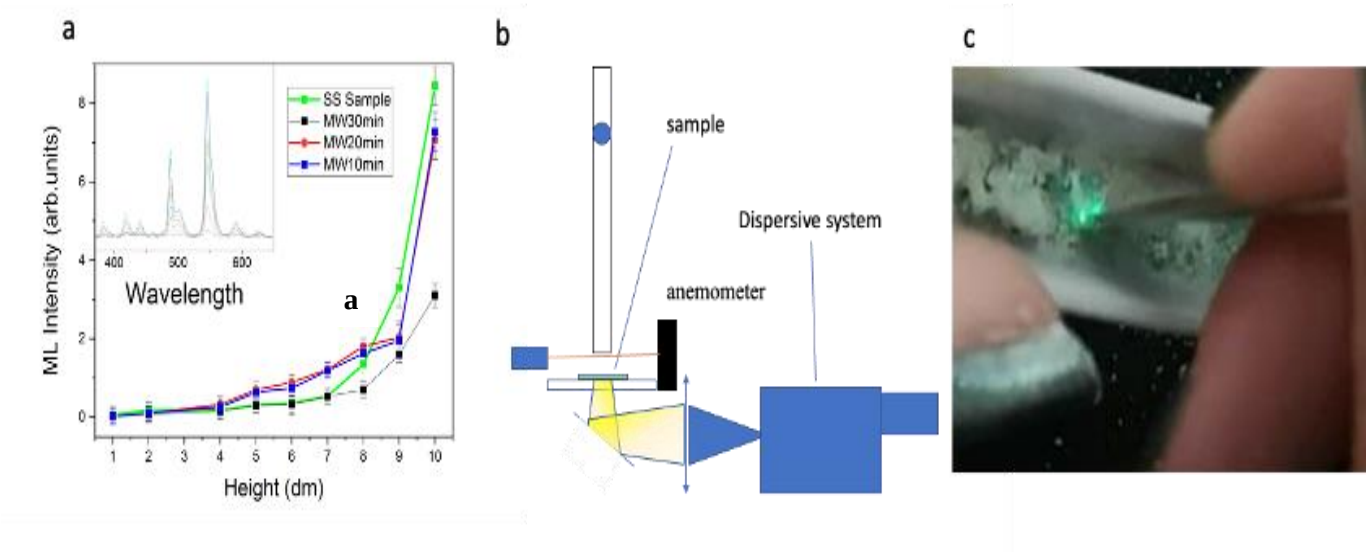

Figure 21. a) Spectral shape of the light emitted (inset) and overall intensity from the peak at 545 nm of the Tb emission as function of the drop height, b) schematic representation of the experimental set-up, c) image of the bright green emission by simple scratching the synthesized powder in an alumina crucible.

As expected, the sample obtained with synthesis time of 10 minutes, produces a lower light intensity from the impacts. The samples synthesized using the MAS method at 20 and 30 minutes show a slightly lower intensity of mechano-luminescence compared to the SS sample, with a reduction of about 15% for the highest energy impact. At intermediate drop heights (between 0.4 and 0.7m), the ML emission intensity for the MW10 and MW20-samples is well above the intensity for the SS-samples, suggestion a lower threshold energy for ML emission.

3.5. Conclusion

In summary, this study demonstrated the potential of CaZnOS: Tb as a high-efficiency, chemically stable, and eco-friendly mechano-luminescent material for use in modern lighting and display technologies. Using various analytical techniques, it was determined that the materials synthesized using MAS had similar structural, morphological, and optical properties to those synthesized using conventional SS methods, but with enhanced mechano-luminescent properties.

While the final structure MAS samples may contain a higher percentage of impurity compounds due to the absence of a strongly reducing atmosphere, the comparable efficiency of its emission upon single impacts suggests that microwave synthesis can still be a viable and advantageous method for certain applications. For example, MAS can offer faster reaction times, higher reaction yields, and greater control over reaction conditions, making it an attractive alternative to traditional SS synthesis. Additionally, MAS can be a more sustainable and energy-efficient process, with reduced solvent and energy consumption compared to other methods. Therefore, despite the presence of impurities, the efficiency of MAS samples indicates that this method has potential for efficient and sustainable synthesis in various fields and for practical applications, however more focalized efforts on the specific performance needs to be performed for a fully optimization of the synthesis conditions.

References

1. Colacino, E.; Carta, M.; Pia, G.; Porcheddu, A.; Ricci, P.C.; Delogu, F. Processing and Investigation Methods in Mechanochemical Kinetics. ACS Omega 2018, 3, 9196–9209, doi:10.1021/acsomega.8b01431.
2. Fiore, C.; Sovic, I.; Lukin, S.; Halasz, I.; Martina, K.; Delogu, F.; Ricci, P.C.; Porcheddu, A.; Shemchuk, O.; Braga, D.; et al. Kabachnik-Fields Reaction by Mechanochemistry: New Horizons from Old Methods. ACS Sustain. Chem. Eng. 2020, 8, 18889–18902, doi:10.1021/acssuschemeng.0c05744.
3. Sović, I.; Lukin, S.; Meštrović, E.; Halasz, I.; Porcheddu, A.; Delogu, F.; Ricci, P.C.; Caron, F.; Perilli, T.; Dogan, A.; et al. Mechanochemical Preparation of Active Pharmaceutical Ingredients Monitored by in Situ Raman Spectroscopy. ACS Omega 2020, 5, 28663–28672, doi:10.1021/acsomega.0c03756.
4. Feng, A.; Smet, P.F. A review of mechanoluminescence in inorganic solids: Compounds, mechanisms, models and applications. Materials (Basel). 2018, 11, 484.
5. Zhuang, Y.; Xie, R.J. Mechanoluminescence Rebrightening the Prospects of Stress Sensing: A Review. Adv. Mater. 2021, 33, 2005925.
6. Yang, X.; Cheng, Y.; Xu, J.; Lin, H.; Wang, Y. Stress Sensing by Ratiometric Mechanoluminescence: A Strategy Based on Structural Probe. Laser Photonics Rev. 2022, 16, 2200365, doi:10.1002/lpor.202200365.
7. Chen, C.; Zhuang, Y.; Li, X.; Lin, F.; Peng, D.; Tu, D.; Xie, A.; Xie, R.J. Achieving Remote Stress and Temperature Dual-Modal Imaging by Double-Lanthanide-Activated Mechanoluminescent Materials. Adv. Funct. Mater. 2021, 31, 6, doi:10.1002/adfm.202101567.
8. Zhuang, Y.; Li, X.; Lin, F.; Chen, C.; Wu, Z.; Luo, H.; Jin, L.; Xie, R.J. Visualizing Dynamic Mechanical Actions with High Sensitivity and High Resolution by Near-Distance Mechanoluminescence Imaging. Adv. Mater. 2022, 34, 2202864, doi:10.1002/ADMA.202202864.
9. Lee, H.B.; Shin, H.G.; Timilsina, S.; Kim, J.; Kim, G.-W. Sound visualization based on mechanoluminescent diaphragms. In Proceedings of the https://doi.org/10.1117/12.2612325; SPIE, 2022; Vol. 12045, p. 34.
10. Zhou, H.; Du, Y.; Wu, C.; Jiang, Y.; Wang, F.; Zhang, J.; Wang, Z. Understanding the mechanoluminescent mechanisms of manganese doped zinc sulfide based on load effects. J. Lumin. 2018, 203, 683–688, doi:10.1016/j.jlumin.2018.07.018.

11. Chen, Y.; Zhang, Y.; Karnaushenko, D.; Chen, L.; Hao, J.; Ding, F.; Schmidt, O.G. Addressable and Color-Tunable Piezophotonic Light-Emitting Stripes. Adv. Mater. 2017, 29, 1605165, doi:10.1002/adma.201605165.

12. Zhang, J.-C.; Xu, C.-N.; Kamimura, S.; Terasawa, Y.; Yamada, H.; Wang, X. An intense elastico-mechanoluminescence material CaZnOS:Mn^2+ for sensing and imaging multiple mechanical stresses. Opt. Express 2013, 21, 12976, doi:10.1364/OE.21.012976.

13. Sambrook, T.; Smura, C.F.; Clarke, S.J.; Kang, M.O.; Halasyamani, P.S. Structure and physical properties of the polar oxysulfide CaZnOS. Inorg. Chem. 2007, 46, 2571–2574, doi:10.1021/ic062120z.

14. Joos, J.J.; Lejaeghere, K.; Korthout, K.; Feng, A.; Poelman, D.; Smet, P.F. Charge transfer induced energy storage in CaZnOS:Mn - Insight from experimental and computational spectroscopy. Phys. Chem. Chem. Phys. 2017, 19, 9075–9085, doi:10.1039/c7cp00285h.

15. Corpino, R.; Angioni, D.; Satta, J.; Ugbo, F.C.; Chiriu, D.; Carbonaro, C.M.; Melis, C.; Stagi, L.; Ricci, P.C. Emission mechanism in single and co-doped Tb:Eu:CaZnOS. J. Alloys Compd. 2021, 868, 159007, doi: 10.1016/j.jallcom.2021.159007.

16. Zhang, Z.J.; Feng, A.; Chen, X.Y.; Zhao, J.T. Photoluminescence properties and energy levels of RE (RE = Pr, Sm, Er, Tm) in layered-CaZnOS oxysulfide. J. Appl. Phys. 2013, 114, 213518, doi:10.1063/1.4842815.

17. Qiu, Z.; Rong, C.; Zhou, W.; Zhang, J.; Li, C.; Yu, L.; Liu, S.; Lian, S. A strategy for synthesizing CaZnOS: Eu2+ phosphor and comparison of optical properties with CaS: Eu^{2+}. J. Alloys Compd. 2014, 583, 335–339, doi: 10.1016/j.jallcom.2013.08.162.

18. Xu, Z.; Xia, Z.; Lei, B.; Liu, Q. Full color control and white emission from CaZnOS: Ce3+,Na+,Mn2+ phosphors: Via energy transfer. J. Mater. Chem. C 2016, 4, 9711–9716, doi:10.1039/c6tc03016e.

19. Yang, Y.L.; Zhou, Y.; Pan, D.J.; Zhang, Z.J.; Zhao, J.T. The luminescence properties of CaZnOS: Bi3+, Sm3+, Li+ phosphors with tunable emissions and energy transfer for white emission. J. Lumin. 2019, 206, 578–584, doi:10.1016/j.jlumin.2018.10.046.

20. Ricci, P.C.; Satta, J.; Chiriu, D.; Corpino, R.; Carbonaro, C.M.; Salis, M.; Melis, C.; Normile, P.S.; De Toro, J.A. Optical and vibrational properties of CaZnOS: The role of intrinsic defects. J. Alloys Compd. 2019, 777, 225–233, doi:10.1016/j.jallcom.2018.10.311.

21. Chiriu, D.; Stagi, L.; Carbonaro, C.M.; Corpino, R.; Ricci, P.C. Energy transfer mechanism between Ce and Tb ions in sol-gel synthesized YSO crystals. Mater. Chem. Phys. 2016, 171, 201–207, doi:10.1016/j.matchemphys.2016.01.006.

22. Ricci, P.C.; Salis, M.; Corpino, R.; Carbonaro, C.M.; Fortin, E.; Anedda, a. A kinetics model for Tb3+ recombinations in low doped Tb: Lu1.8Y0.2SiO5 crystals. J. Appl. Phys. 2010, 108, 1–7, doi:10.1063/1.3467788.

23. Tu, D.; Xu, C.N.; Fujio, Y.; Yoshida, A. Mechanism of mechanical quenching and mechanoluminescence in phosphorescent CaZnOS:Cu. Light Sci. Appl. 2015 411 2015, 4, e356–e356, doi:10.1038/lsa.2015.129.

24. Miranda de Carvalho, J.; Pedroso, C.C.S.; Saula, M.S. de N.; Felinto, M.C.F.C.; de Brito, H.F. Microwave-assisted preparation of luminescent inorganic materials: A fast route to light conversion and storage phosphors. Molecules 2021, 26, 2882.

25. Perera, S.S.; Munasinghe, H.N.; Yatooma, E.N.; Rabuffetti, F.A. Microwave-assisted solid-state synthesis of NaRE(MO4)2 phosphors (RE = La, Pr, Eu, Dy; M = Mo, W). Dalt. Trans. 2020, 49, 7914–7919, doi:10.1039/D0DT00999G.

26. Kitchen, H.J.; Vallance, S.R.; Kennedy, J.L.; Tapia-Ruiz, N.; Carassiti, L.; Harrison, A.; Whittaker, A.G.; Drysdale, T.D.; Kingman, S.W.; Gregory, D.H. Modern microwave methods in solid-state inorganic materials chemistry: From fundamentals to manufacturing. Chem. Rev. 2014, 114, 1170–1206, doi:10.1021/CR4002353.

27. Fathy, M.; Hassan, H.; Hafez, H.; Soliman, M.; Abulfotuh, F.; Kashyout, A.E.H.B. Simple and Fast Microwave-Assisted Synthesis Methods of Nanocrystalline TiO2and rGO Materials for Low-Cost Metal-Free DSSC Applications. ACS Omega 2022, 7, 16757–16765, doi:10.1021/acsomega.2c01455.

28. Bi, J.; Sun, L.; Wei, Q.; Zhang, K.; Zhu, L.; Wei, S.; Liao, D.; Sun, J. Rapid ultrasonic-microwave assisted synthesis of Eu3+ doped Y2O3 nanophosphors with enhanced luminescence properties. J. Mater. Res. Technol. 2020, 9, 9523–9530, doi:10.1016/j.jmrt.2020.06.056.

29. Cheng, Q.; Kang, M.; Wang, J.; Zhang, P.; Sun, R.; Song, L. Low temperature microwave solid-state synthesis of CaCO3: Eu3+, K+ phosphors. Adv. Powder Technol. 2015, 26, 848–852, doi:10.1016/j.apt.2015.02.010.

30. Lim, C.S.; Aleksandrovsky, A.; Molokeev, M.; Oreshonkov, A.; Atuchin, V. Microwave sol-gel synthesis and upconversion photoluminescence properties of CaGd2(WO4)4:Er3+/Yb3+ phosphors with incommensurately modulated structure. J. Solid State Chem. 2015, 228, 160–166, doi:10.1016/j.jssc.2015.04.032.

31. He, C.; Xia, Z.; Liu, Q. Microwave solid state synthesis and luminescence properties of green-emitting Gd2O2S:Tb3+ phosphor. Opt. Mater. (Amst). 2015, 42, 11–16, doi:10.1016/J.OPTMAT.2014.12.012.

32. Miranda De Carvalho, J.; Van Der Heggen, D.; Martin, L.I.D.J.; Smet, P.F. Microwave-assisted synthesis followed by a reduction step: Making persistent phosphors with a large storage capacity. Dalt. Trans. 2020, 49, 4518–4527, doi:10.1039/d0dt00416b.

33. Lutterotti, L. Total pattern fitting for the combined size–strain–stress–texture determination in thin film diffraction. Nucl. Instruments Methods Phys. Res. Sect. B Beam Interact. with Mater. Atoms 2010, 268, 334–340, doi:10.1016/J.NIMB.2009.09.053.

34. Ricci, P.C.; Carbonaro, C.M.; Corpino, R.; Cannas, C.; Salis, M. Optical and structural characterization of terbium-doped Y 2SiO5 phosphor particles. J. Phys. Chem. C 2011, 115, 16630–16636, doi:10.1021/JP203523S/SUPPL_FILE/JP203523S_SI_001.PDF.

35. Li, M.; Wang, L.; Ran, W.; Deng, Z.; Shi, J.; Ren, C. Tunable Luminescence in Sr2MgSi2O7:Tb3+, Eu3+Phosphors Based on Energy Transfer. Mater. 2017, Vol. 10, Page 227 2017, 10, 227, doi:10.3390/MA10030227.

36. Pan, C.; Zhang, J.C.; Zhang, M.; Yan, X.; Long, Y.Z.; Wang, X. Intrinsic oxygen vacancies mediated multi-mechano-responsive piezoluminescence in undoped zinc calcium oxysulfide. Appl. Phys. Lett. 2017, 110, 233904, doi:10.1063/1.4985012.

37. Lakowitz, J.R. Energy Transfer. In Principles of Fluorescence Spectroscopy; Springer US, 2006; pp. 443–475.

Synergistic Effects of Tb^{3+} in Long-Persistent Luminescence in $Ca_3Ga_4O_9$: xBi^{3+}, yZn^{2+} Phosphors: Implications for Novel Optical Materials

4.1. Abstract

Phosphor materials are an emerging class of compounds with a promising potential for advancing optical data storage technology. In this study, we synthesized and conducted a thorough characterization of $Ca_3Ga_4O_9$: xBi^{3+}, yZn^{2+}, zTb^{3+} (hereafter CGO) phosphors doped with different levels of Tb^{3+} ions.

The goal of our investigation was to gain a deeper understanding of the impact of Tb^{3+} doping on the optical and structural properties of the material. Overall, this study provides a comprehensive insight into the properties of long-persistent phosphors and demonstrates their potential for various technological applications, including optical data storage.

4.2. Introduction

Long Persistent Luminescence Phosphors (LPLPs) are a type of phosphor material that can store and emit light over a prolonged period, after the excitation source has been removed. Excitation source might emerge from plasma beam UV radiation, visible light, X-rays, γ-rays, or electron beam [1] Because of its unique ability to store and release photo excited carriers, long persistent phosphorescence (LPP) is crucial in various fields, such as spectroscopy, photochemistry, photonics, and materials science. Inorganic LPLP are essentially composed of a host matrix, often highly defective, which acts crucially as either an originator or emitting centres or intentionally doped with elements to introduce levels in the host band gap, and with luminescent ions. The emission spectrum of LPLP is determined by the combination of the energy levels of the host/impurities (trapping site) and those of the dopant luminescent ions. [2-4] When the excitation is interrupted, the traps are slowly emptied. This gradual emptying leads to the persistent luminous emission that characterises these materials and depends on the depth of the traps. Some of well-known luminescence centres for persistent luminescent includes $Eu^{2+,}$ $Pr^{3+,}$ $Eu^{3+,}$ $Tb^{3+,}$ $Mn^{2+,}$ $Ti^{3+,}$ $Cr^{3+,}$ Bi^{3+}, Pb^{2+}, Eu3+, Eu^{2+}, $Ce^{3+,}$ Mn^{3+} etc, often present in the host matrix as doping substitutional element.

The first literature work on persistent phosphors dates to 1994 [5-7] then since 1996, research in this field has shown a strong growth represented by 250 publications per year.[8]. Recently, alkaline-earth metal gallate compounds have received particular attention as host materials for long persistent phosphors due

to their high stability and ability to harmonise with different categories of dopants (rare-earth and metals and non-metals) because of its crystal structure.

A promising matrix for its optical and structural properties is $Ca_3Ga_4O_9$, a wide band-gap material (4 eV) with a valence band dominated primarily by the 3p states of calcium and the 2s 2p states of oxygen, while the conduction band is dominated by the 4s 4p states of gallium. [9]. The $Ca_3Ga_4O_9$ crystallizes in the Cmm2 space group in the orthographic configuration with cell dimensions of a=14.374 Å, b=16.810 Å, and c=5.3082 Å.

Several studies have shown that synthesis approach can affect the structural and the optical properties of a material, it is pertinent to adopt suitable means of synthesis that will avoid further thermal treatment. Many methods exist for the growth of LPLP such as sol-gel [10], Chemical precipitation from homogeneous solution [11], hydrothermal strategy [12], ultrasonic assisted strategy [13] but for the purpose of this study, solid state was utilized to develop plain CGO and doped with different levels of Tb^{3+}. Solid-state has proven to be one of the best methods to obtain high-purity crystalline host with well blend activators and fluxes of the composites powers without needing any after synthesis treatment measures. In this work we investigated with a multi-technique approach, how different doping percentages of Tb^{3+} ions can influence the optical properties of the material. Terbium was chosen mainly because it exhibits a strong green luminescence due to 5d transitions, which is particularly advantageous since the human eye is very sensitive to these wavelengths [14].

Structural characterization (X-ray and Raman spectroscopy) to optical properties (static and time-resolved luminescence, thermoluminescence, and phosphorescence), provide a comprehensive understanding of the structural and optical properties of Tb doped $Ca_3Ga_4O_9$ material as long-persistent phosphors.

4.3. Materials and methods

4.3.1. **Materials**

$CaCO_3$ (CAS No.: 471-34-1), Ga_2O_3 (CAS No.: 12024-21-4), Bi_2O_3 (CAS No.: 1304-76-3), ZnO (CAS No.: 1314-13-2), and Tb_4O_7 (CAS No.: 12037-01-3) were purchased from Sigma Aldrich. All chemicals were used as received without further purification.

4.3.2. Synthesis Procedure

The $Ca_3Ga_4O_9$: xBi^{3+}, yZn^{2+}, zTb^{3+} samples were prepared by a high-temperature solid-state synthesis.

$$3CaCO_3 + 2Ga_2O_3 + xBi_2O_3 + yZnO + zTb_4O_7 \rightarrow Ca_{(3-x-z)}\ Ga_{(4-y)}\ O_9{:}Tb3^{+} \quad (8)$$

Due to the similarity of their ionic radii, the Bi^{3+} cation (r = 1.03 Å) substitutes for the Ca^{2+} cation (r = 1.00 Å) in the crystal structure. Similarly, the Tb^{3+} cation (r = 0.92 Å) substitutes for the Ca^{2+} cation. As for the Zn^{2+} cation (r = 0.6 Å), having an ionic radius more like that of the Ga^{3+} cation (r = 0.47 Å), it was substituted for the latter.

The precursors, in the correct amounts, were first mixed in an agate mortar and then subjected to a heat treatment of 1200°C for 10 hours. For the synthesis of the materials, the percentages of Bi^{3+} and Zn^{2+} were kept constant while the doping percentages with Tb^{3+} were varied between 2% to 8% wt.

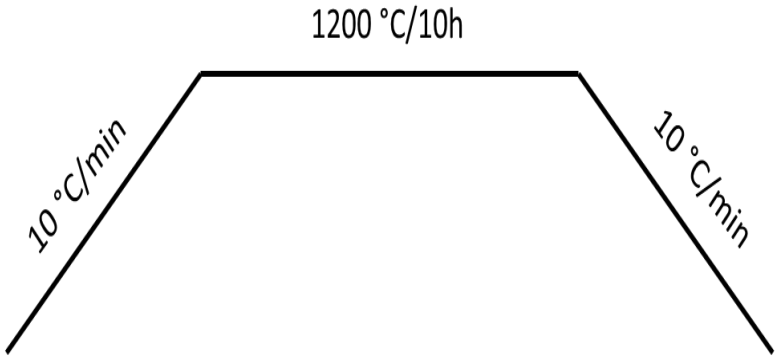

Figure 22. Schematics of the heat treatment of all the CGO samples.

4.4. Characterization Techniques

X-ray diffraction measurements were conducted using a Bruker D8 Advance diffractometer operating at 30 kV and 20 mA. The diffractometer was equipped with a Cu tube as the X-ray source (wavelength of 1.5418 Å) and a Vantec-1 PSD detector. The powder patterns were collected in the 2θ range of 10° to 70°.

Raman spectroscopy measurements were performed using an MS750 spectrograph (Sol-Instruments) equipped with a 600 gr/mm grating. A 785 nm laser was used as the excitation source, focused through

a 10X Olympus objective lens with an estimated laser power of $1x10^{-2}$ W/cm^2. No heating effect on the samples has been revealed. The measurements were conducted at room temperature, with a spectral resolution of 1cm^{-1}.

Steady time photoluminescence measurements were performed using an MS750 spectrograph (Sol-Instruments) equipped with a 175 gr/mm grating. A 405 nm laser was used as the excitation source, focused through a 10X Olympus objective lens.

Time-resolved luminescence characteristics were achieved employing an optical parametric oscillator with a frequency doubler device, pumped with third harmonic (355 nm) of a pulsed Nd: YAG laser (Quanta Ray Pro 730). The excitation pulse width at half-maximum was 8 ns with a repetition rate of 10 Hz, and a spectral bandwidth less than 0.3 cm^{-1}. Signals achieved was distributed with spectrograph (Arc-SpectraPro 300i) of spectral bandpass less than 2.5 nm and detected by a gateable intensified CCD (PI MAX Princeton Inst.). To reduce the dark current, the detector was allowed to cool down to -20°C with the aid of a Peltier device.

Thermoluminescence measurements were performed using a Homemade thermoluminescence system composed by a heating system controlled with a programmable power supply (Agilent 6030A), 0-200V/0-17A, 1000W and Phototube detector coupled with a high sensitivity data acquisition and control unit HP 3852A. The measurements were performed in a range between RT and 523 K with a heating rate of 10°C/min controlled by LabVIEW 2019 homemade routine.

Phosphorescence measurements were performed at 20°C monitoring the overall emission 1 per second with accumulation time of 100 ms for each measure.

4.5. Results and Discussion

To identify and to study the crystal structure of the obtained materials, a reference matrix underwent quantitative analysis using the Rietveld method, which allowed to identify the present phases and determine their percentage quantities using MAUD software. As reference diffraction patterns to compare with the measured diffraction pattern, CIF files obtained from the Crystallography Open Database were used. From the XRD analysis of the sample used as a matrix, we observed the presence of two phases whose geometric characteristics are reported in Table 3. The main phase is $Ca_3Ga_4O_9$ in its orthorhombic reference phase, with minor peaks related to the secondary phase $CaGa_2O_4$, in the

orthorhombic phase. In $Ca_3Ga_4O_9$, the GaO_4 tetrahedra and calcium cations are arranged in layers. There are four crystallographic sites for Ca^{2+} which we will refer to as Ca_1, Ca_2, Ca_3, and Ca_4. The Ca_1 and Ca_3 atoms are arranged in an orthorhombic configuration surrounded by six oxygen atoms, while Ca_2 and Ca_4 are surrounded by eight oxygen atoms. The refined diffraction pattern (Figure23) shows the presence of relative residuals mainly attributed to the observed minority phase peaks but exhibits excellent agreement between the observed and calculated diffraction pattern.

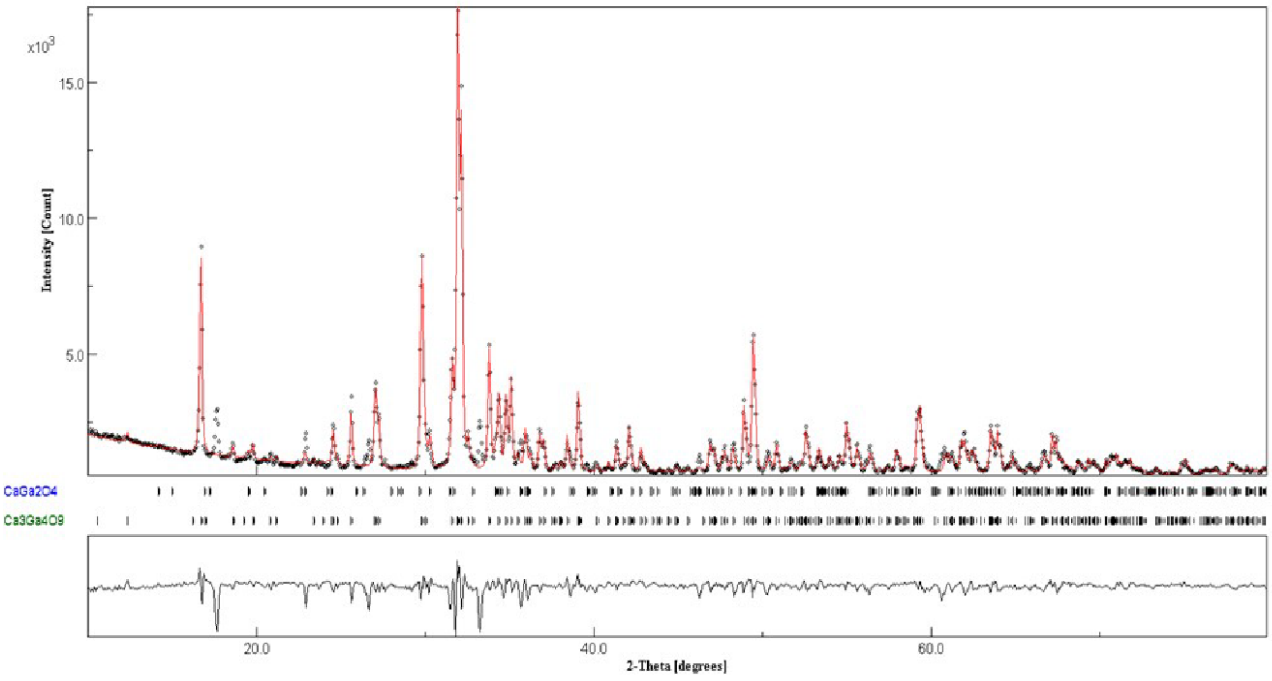

Figure 23. X-Ray diffraction pattern of CGO: Tb^{3+}

Table 3. Phases from XRD Refinement

Phases	a[Å]	b[Å]	c[Å]
$Ca_3Ga_4O_9$ orthorombic phase (Cmm2) 93%	14.374	16.810	5.3082
$CaGa_2O_4$ orthorombic phase (Pna21) 6.1%	10.234	7.759	9.160

Table 3 Phases from XRD Refinement

The Raman spectrum of the CGO matrix is shown in Figure 24, providing further insights into both the structural and vibrational properties. It comprises of numerous sharp bands covering the spectral range between 40cm^{-1} to 800cm^{-1}. The most prominent bands reside at 121 and 545cm^{-1}, with a broad structure with two main peaks centred at 675cm^{-1} and 702 cm^{-1}, respectively. Intense bands are located at 89, 180, 243, in conjunction with several other weaker but sharp bands. The band at 545cm^{-1} have shoulders at both the side (approximatively at 485, 515 and 580 cm^{-1}).

Since no Raman data or computational analysis on this compound has been published to date, the assignment of the main vibrational modes has been performed by the studies of similar structures and on the general position on the bands, however a detailed analysis is mandatory, but it is out of the scope of the present work.

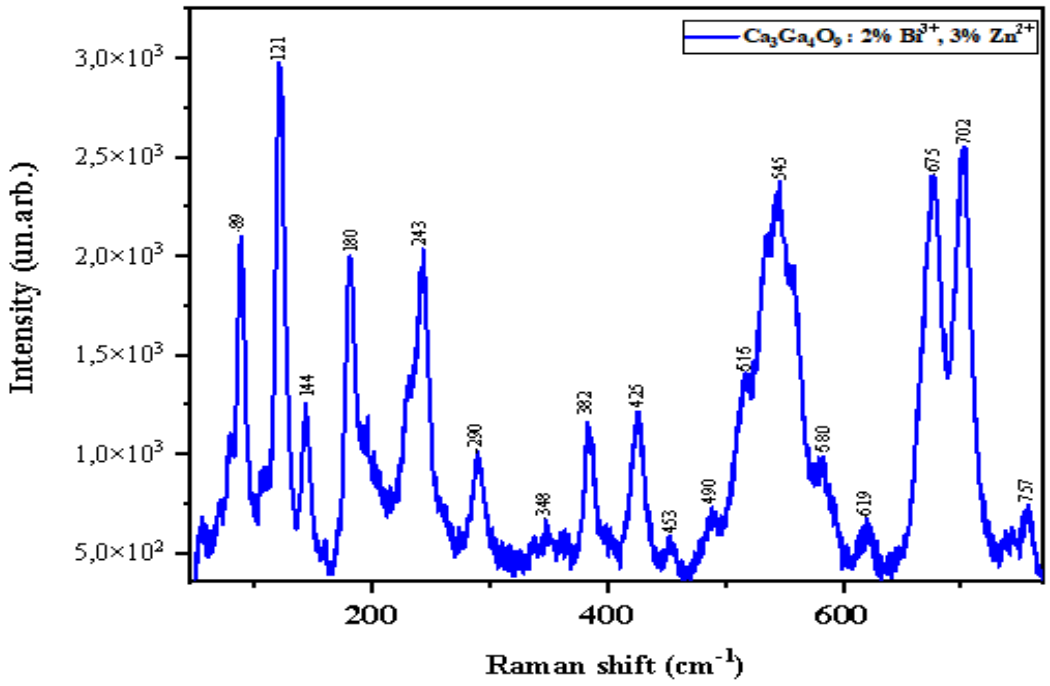

Figure 24. Raman spectrum of CGO matrix

The $Ca_5Ga_6O_{14}$ is an orthographic structure were similarly to CGO, layers of tetrahedral rings are the main building unit. Both compounds can be regarded as tetrahedral layer structures with the calcium cations residing between the sheets where Ga^{3+} and Ca^{2+} form four (GaO_4) and six coordination (CaO_6) with the surrounding O^{2-}, respectively. Further, in the CGO structure, there are two additional Ca sites bonded to eight oxygen (CaO_8) in a larger environment. The GaO_4 tetrahedra generate the band at 545,

675 and 757 cm^{-1} (bending and stretching of GaO_4 units). Further assignments concern the modes at lower wavenumber that involve the collective motion O-Ga-O among different tetrahedra structures and the mode at 121 cm^{-1} ascribed to the Ca-O bond. Finally, the intense modes at 290 and 702 cm^{-1} are assigned to the bending and stretching vibrational mode of the $Ca\text{-}O_8$ units.

This last mode suffers of the main variation with the increasing with Tb doping. In Figure 25 it can be observed that the increase of Tb ions produces a shift towards the low wavenumber of the band (progressively from 702 to 704 cm^{-1}) and a significant decrease of the relative Raman intensity (from 1.05 in the CGO matrix down to 0.75 in the sample Tb doped with the highest percentage). On the other hand, despite the similar ionic radius between Ca^{2+} and Tb^{3+} (1.02 A° and 1.18 A°) there is a significant variation in the ionic mass from 40 to 170.9 and a distortion of the structure due to the different charge and the formation of vacancy sites. Similarly, the substitution of Ca with Tb, generate a variation in the mode at 121 cm^{-1} with a progressive shift to 118 cm^{-1}.

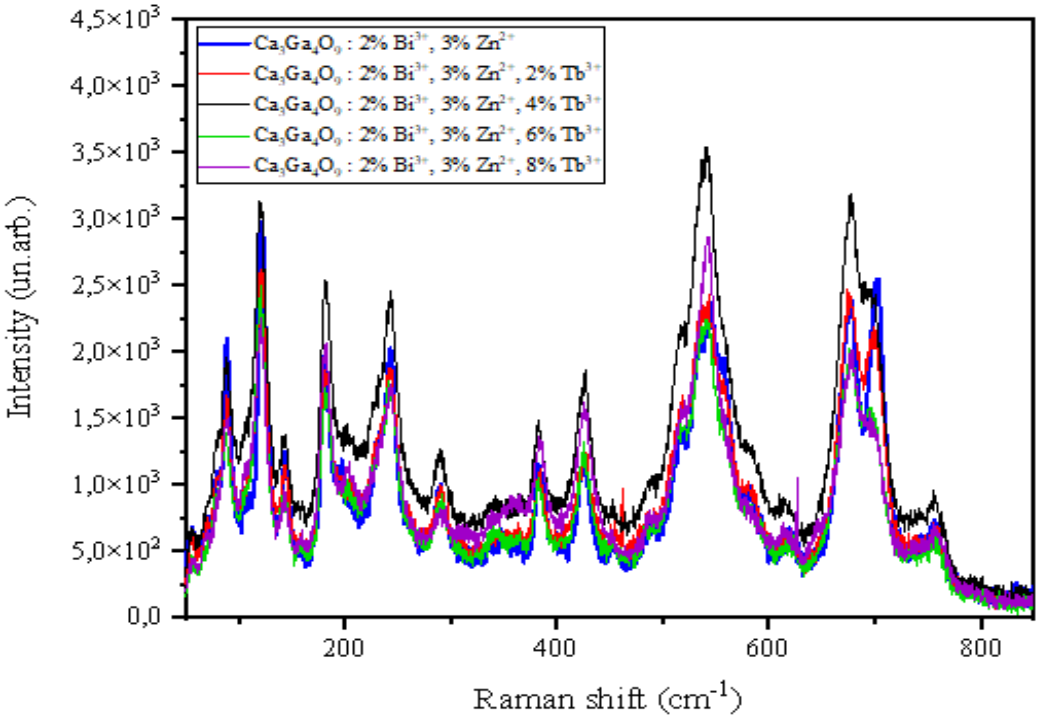

Figure 25. Raman spectra of CGO doped with different percentages of Terbium.

The presence of Bi and Zn are easy to observe for steady time luminescence spectra shown in Figure 26. The presence of Bi^{3+} generates an intense and broad luminescence band at a about 530 nm. When the Bi^{3+} ion occupies the position of the Ca^{2+} ion, the charge is not balanced inducing the distortions in the local symmetry of the Bi^{3+} optical centres. The presence of Zn^{2+} can therefore balance the charge. The process can be described by equation 9.

$$Bi^{3+}+Zn^{2+} = Ca^{2+}+Ga^{3+} \quad (9)$$

Obviously, Zn ions enter in the crystal structure at the Ga site, further generating structural distortion and increasing the charge trapping and, therefore, the persistent emission.

The Tb doped samples still present the broad emission from the defective matrix, but the characteristic Tb emission band are clearly visible: 478 nm, 542 nm, 586 nm e 621 nm, due to the recombination from the $^5D_4 \rightarrow {}^7F_J$ levels (J= 3 to 6, respectively).

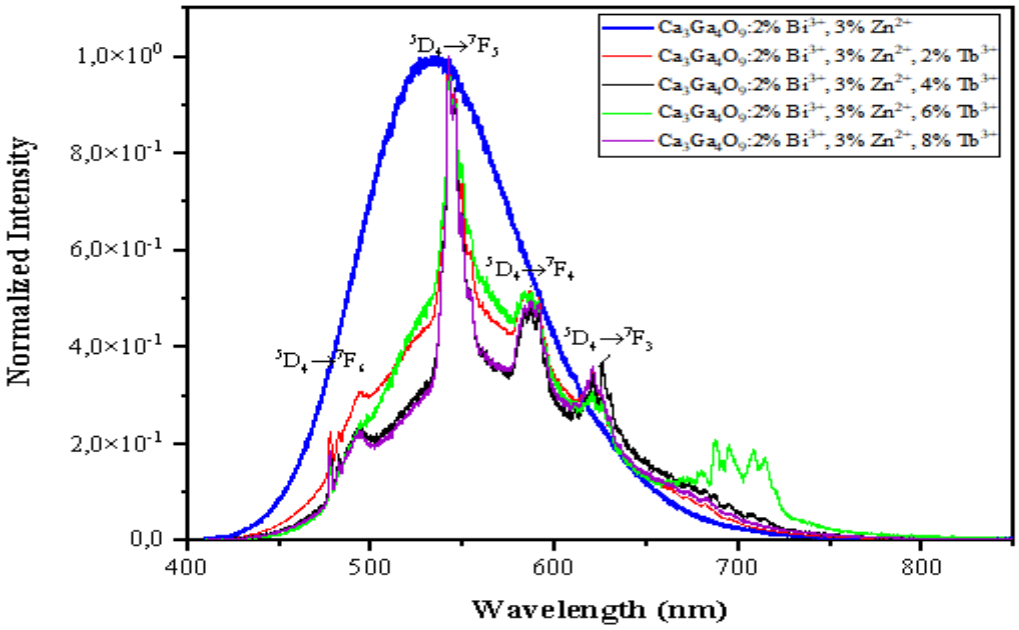

Figure 26. PL spectra of CGO matrix and CGO doped with different percentages of Terbium.

A clear picture of the optical properties of the samples is visible in the 3D plot of the excitation and emission properties of the different samples as displayed by Figure 27. The broad band generated at the Bi^{3+} sites is excited at about 350 nm and introduce an additional excitation channel for the recombination

at the Tb sites. It is worth noting that the overall intensity of the luminescence peaks does not grow asymptotically but it presents a maximum for the sample with 4% Tb doping concentration (Zn 3%, Bi 2%).

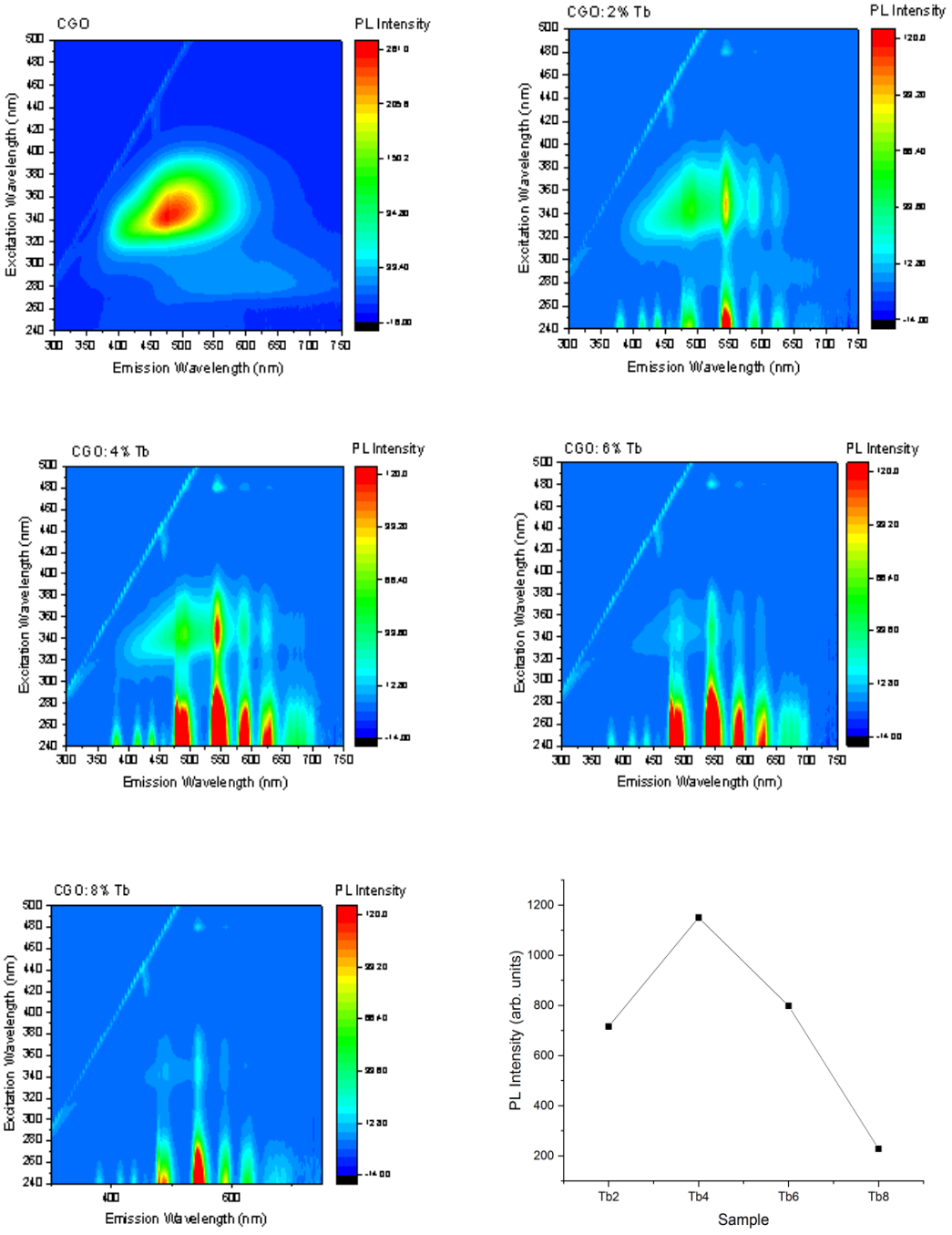

Figure 27. 3D plot of the excitation and emission properties of the different samples

The emission quenching of the luminescence due to the rare earth elements concentration is owing to the resonant transfer of energy between Tb^{3+} ions and can be verified by time resolved luminescence measurements as presented by Figure 28. The time behaviour progressively shifts to faster rate with the Tb concentration, however, due to the intrinsic presence of several defective sites the kinetics cannot be considered with single behaviour but a more complex one, due to the presence of various non-radiative recombination pathways. The decay process can be represented with a multiexponential curve where the time decay can be represented with an average lifetime as shown in equation 10.

$$\tau = \frac{\int_0^\infty I(t) \cdot t dt}{\int_0^\infty I(t) dt} \qquad (10)$$

Where I(t) is the time-dependent photoluminescence intensity.

The calculated lifetime slowly decreases from 2823μs in the 4% to 2796 to 2770 and to 1861μs as the Tb concentration passes from 6%, 2% and 8%, respectively.

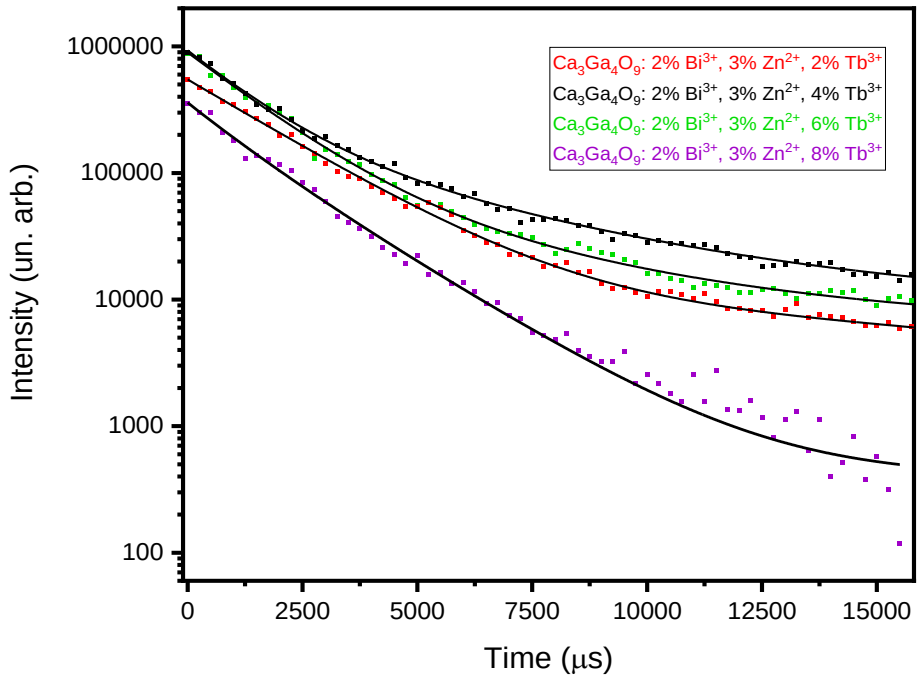

Figure 28. Decay time plots of CGO samples with different percentage of Terbium doping (exc 250 nm)

Thermoluminescence measurements give important insights on the effect of the dopant ions in the matrix and about energy dept in the host band gap. Figure 29 and 30. reports the glow curve for different samples with different doping elements. In the panels, the shape of the thermoluminescence curves have been provided for a better understanding of the experimental measurements. As indicated in the experimental section, all the curves have been obtained after a prolonged excitation at 250 nm (about 4.9 eV, above the matrix band gap). for the charge balance of the two doping ions and for the different substitutional sites (Ca and Ga for Bi and Zn, respectively). On the other hand, the role of Zn in the CGO co-doped with Bi and Zn is mainly to increase the emission efficiency and to decrease the defectivity of the phosphor.

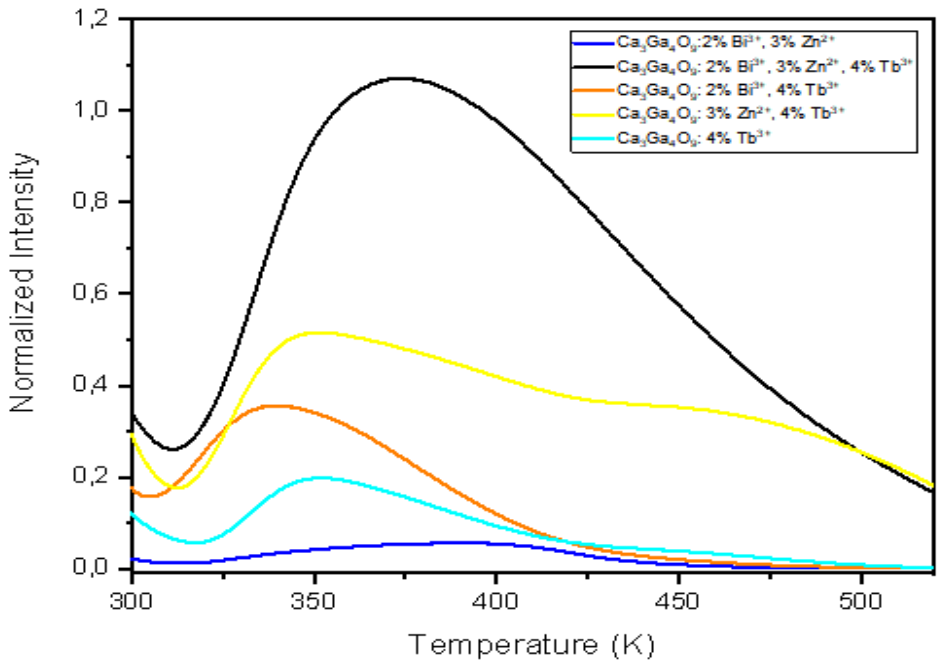

Figure 29. Thermoluminescence measurements of CGO samples

The role of Tb^{3+} in the CGO matrix is very similar to the role of Bi^{3+} for the similar ionic radius and for the same valence charge and as a consequence for the same substituting site (Ca_3 and Ca_4, already discussed in the Raman) as can be verified in the co-doped CGO: Tb^{3+}: Bi^{3+} and CGO: Tb^{3+}, but with a

significant increase of the intensity in the Tb^{3+} doped sample. The fully doped sample (Zn^{2+}, Bi^{3+} and Tb^{3+}) provides the thermoluminescence curve with the highest intensity.

This point can be due apart to the overall increasing of the dopant centers even to an increased efficiency in the radiative recombination path in the rare earth.

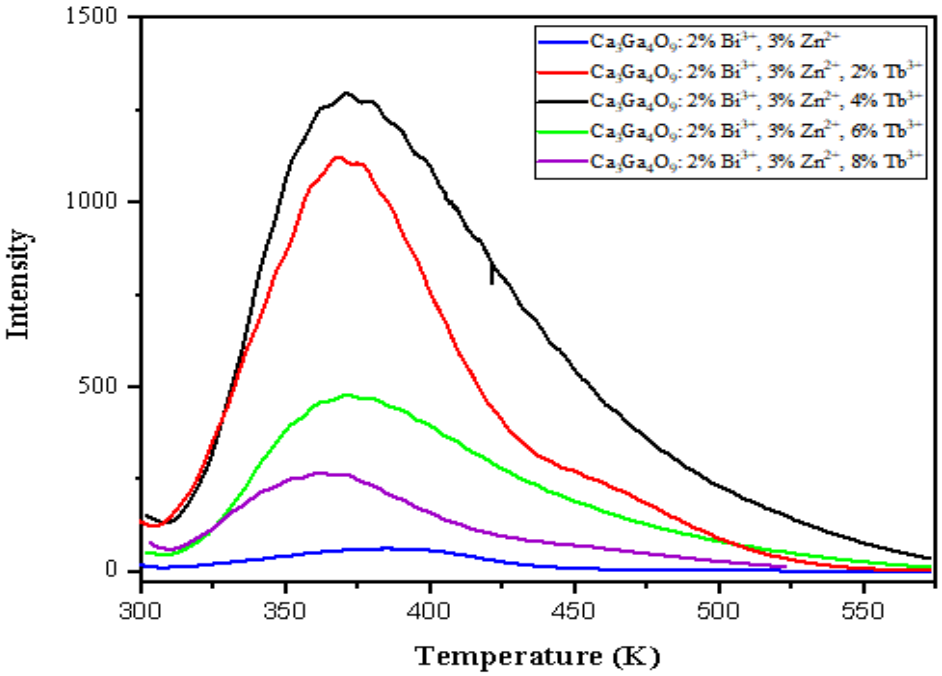

Figure 30. Thermoluminescence CGO different Tb^{3+} concentration

To better provides further insights and considering the presence of three main contribution in the thermoluminescence curve, it is possible to apply the generalized order of kinetic model (GOK) to the TL experimental curve, considering that the thermal response can be described by the superposition of three components as shown by equation 11.

$$I(T) = \sum_{j=1}^{n} A_j * S_j exp\left(\frac{E_j}{KT}\right) \times \left[I * \frac{(b_j - I)S_j}{\beta} \int_{t_1}^{t_2} exp\left(-\frac{E_j}{KT}\right) dt\right]^{\frac{b_j}{b_{j-j}}} \quad (11)$$

where A is a proportionality constant, which depends on the traps concentration, E is the thermal trap depth (the thermal energy needed to release the trapped charge carrier that can be different from the optical energy needed to release the trapped carrier), K_B is Boltzmann's constant, b and S are phenomenological parameters related to the trapping kinetics and frequency factor respectively, and β is the sample heating rate (10 K/s). Second order kinetics (or bimolecular) typically arises when there is a

high probability of re-trapping the released electrons with respect to the recombination at the luminescent centre while the frequency factor S (or ‘‘attempt- to-escape’’ frequency) has the physical meaning of the number of times per second that a bound electron interacts with the lattice phonons. Increasing the Tb^{3+} content in the host matrix the glow peak in the thermoluminescence measurements produce a variation in the overall intensity without alter the curve shape and hence the defect types and relative ratio among them. As already observed in the PL measurements, the sample with the highest emission is the sample doped at 4%, increasing the doping content produce a progressive decrease due to the resonant charge transfer among the Tb^{3+} ions. (Figure 31)

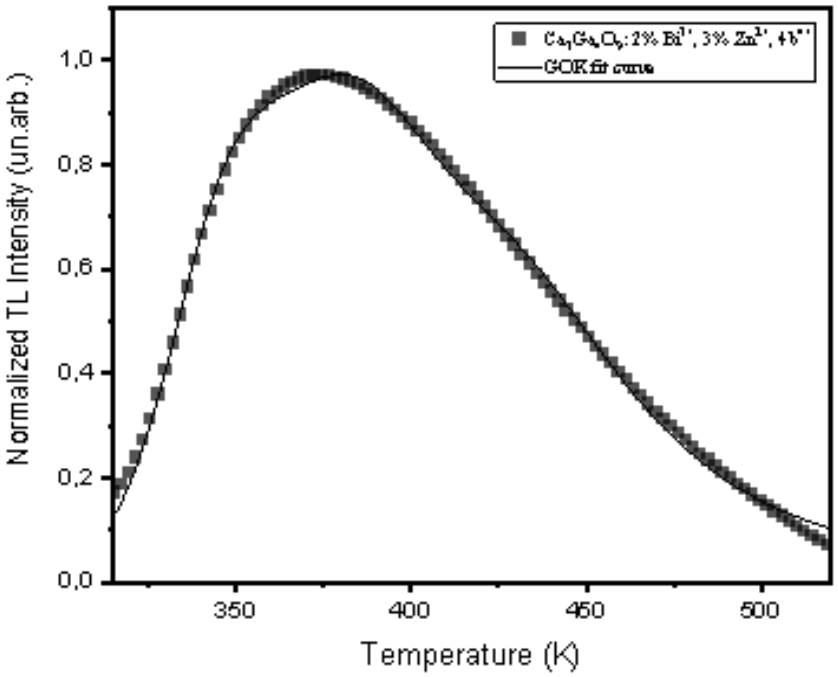

Figure 31. GOK curve.

The results, indicated in table 4 points out the energy of the traps, at 0.83, 0.85 and 0.89 eV assigned to hole traps at the Ga vacancies, and deeper electron trap related to the substitution of Ca with trivalent ions Tb^{3+} ions and Bi^{3+} respectively. Most probably the defect centre created are related to oxygen vacancies, and the formation of F+ centre or F centre depending on the number of electrons trapped. Since the depth of the trapping potential for the electrons in the F+ centers in oxides are deeper than that in F centers the two peaks with different trapping depths in the thermoluminescence curve will be detected.

A_j	186.56461 ± 2.5459
A_j	2 ± 0.3
S_j	3.3984E10 ± 3.60477E10
E_j	0.84634 ± 0.03102
A1	305.14904 ± 2.23923
b_j	2 ± 0.3
S_j	2.30958E9 ± 1.9225E9
E_j	0.85025 ± 0.02598
A2	108.05407 ± 3
b2	2 ± 0.3
S2	1.20398E8 ± 3.17539E6
E2	0.89 ± 0.03

Table 4 parameters of the TL fit.

Bi^{3+} and Tb^{3+} substitution contribute to the formation of defect clusters in the proximity of the dopant: $Tb^{3+}{}_{Ca}$-V_0 and $Bi^{3+}{}_{Ca}$-V_0 acting as electron trapping centers with both Tb^{3+} and Bi^{3+} as the emission centers. Further, the formation of clustered defects favours the occurrence of the tunnelling process, related on the distance between the involved centers and hence, of the doping percentage. On the other hand, since the capability of a dopant cation to delocalize its electron density to stabilize an empty anion vacancy increases with the reduction of its ionizing potential, it is expected that Tb^{3+} has a stronger affinity to attract an anion vacancy (oxygen defect cluster), with respect Bi^{3+}. Consequently, Tb^{3+} stabilizes the energy of the associated trapped electron generating a greater efficiency. This effect can be observed in the PL behaviour upon excitation with band-to-band excitation as indicated in figure 32. In this condition a broad emission at about 400 nm can be observed, that, considering it is common to the all the samples (CGO: Zn^{2+}: Bi^{3+} :Tb^{3+}, CGO:Zn^{2+}: Bi^{3+}, CGO:Zn:Tb^{3+}, CGO:Bi:Tb^{3+}), it can be directly related to recombination at the defect sites. Time resolved measurements show a very fast and efficient transfer to the Tb^{3+} sites, clearly indicating the fundamental role in the optical process of the rare earth.

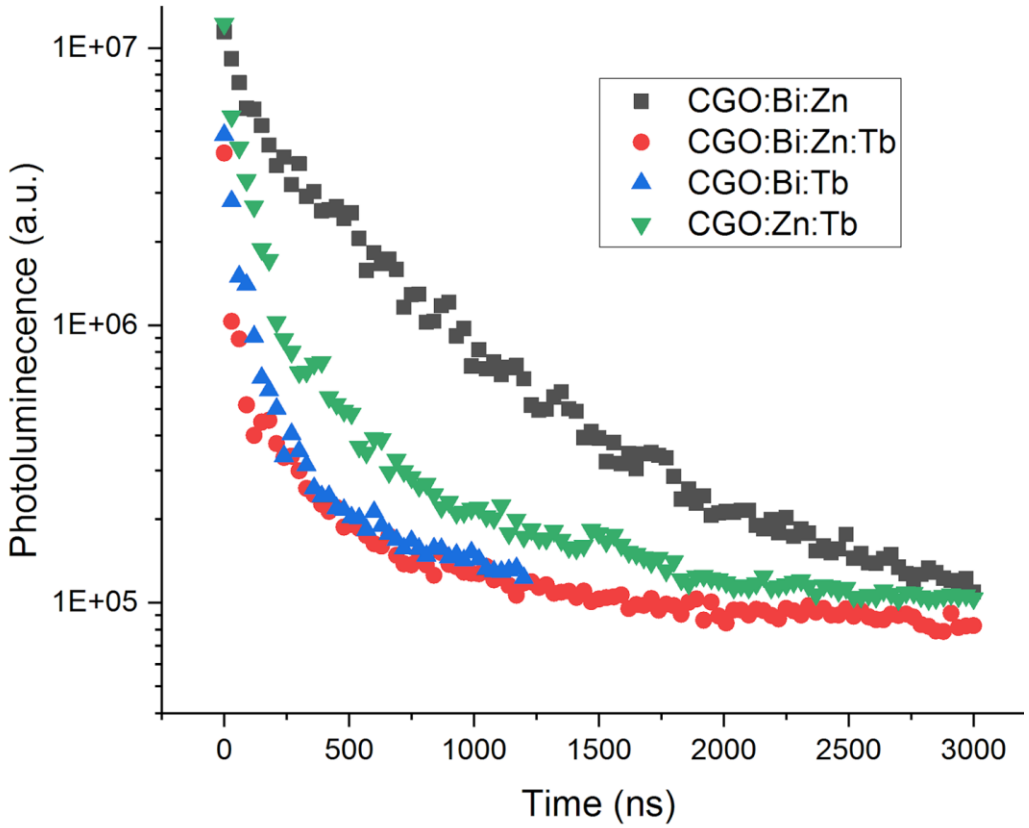

Figure 32. Time resolved measurements (exc. 250 band at 400 nm)

A confirmation about the nature of the defects and the general role of the dopant can be obtained by the analysis of the optical behaviour of the different samples with intraband excitation energy. In particular, the excitation channel indicated in the PLE curves has been utilized and a broad band centered at about 500 nm with excitation at 355 nm has been observed. According to previous reports, the intensity of the band is highly increased in the sample containing Zn^{2+} and Bi^{3+}, in respect to the sample doped with only Bi^{3+}. The time scale domain utilized, well focalize on this band, and the emissions from Tb^{3+} ions do not appear (time delay 20-time window 20ns). As already pointed out, the recombination from the D level of Tb^{3+} have a time decay constant on the order of hundreds of microseconds to ms and are not visible in short time scale). The broad band has been assigned to recombination at the luminescence centers related to Bi^{3+} ions in distinct crystallographic sites: Bi^{3+} ions replacing Ca in the CaO_6 site and in CaO_8 as in Figure 33.

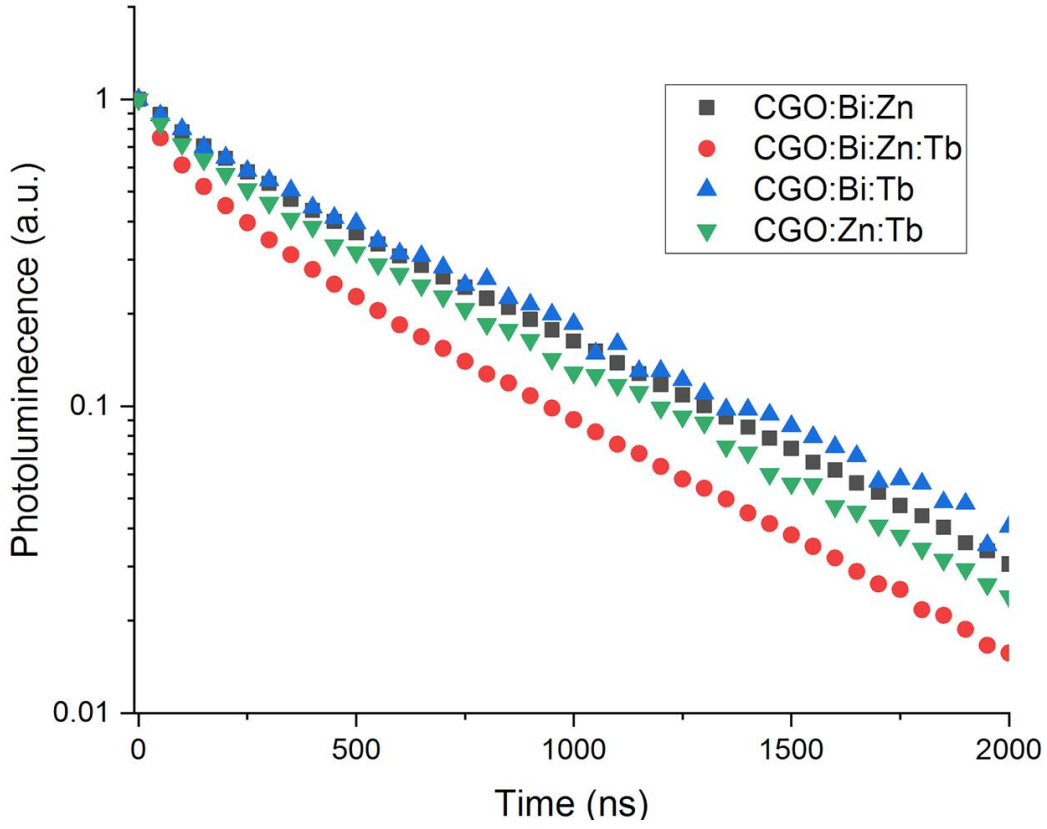

Figure 33. Time resolved measurements (exc 355 band at 500 nm)

also, formation of each defect is a function of several parameters, not only on the doping procedure but also on the synthesis procedure. Time, temperature, and atmosphere play a fundamental role mainly on the distribution of the oxygen vacancies in the host crystal and minor variation in different experimental set up can produce minor variation in the relative peak intensities of the thermoluminescence and photoluminescence curve, but obviously not their energy position in the band gap.

The presence of a very high concentration of filled trap at room temperature upon UV excitation, generates an intense afterglow or persistence. Figure 34 shows the long-lasting phosphorescence acquired after 3 hours from the illumination, clearly indicating the higher efficiency of the Tb^{3+} doped samples with respect the samples doped with only Bi and/or Zn. It is interesting to note that the spectral shape remains unvaried, resembling the recombination at the Tb^{3+} site. No signal in the thermoluminescent curve after the LPL decay has been detected showing that the defect sites are in contact each other.

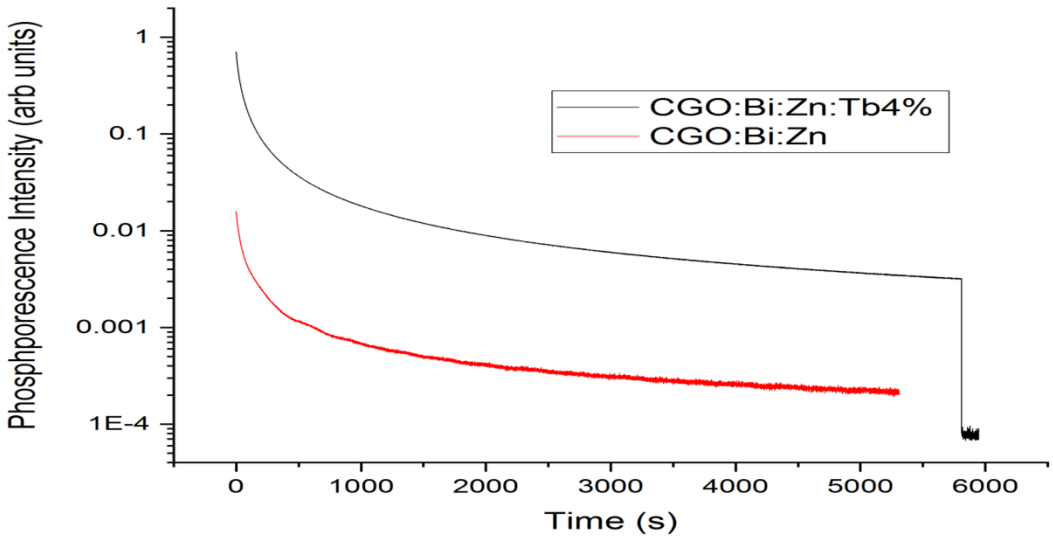

Figure 34. Phosphorescence

4.6. Conclusion

In summary, high temperature solid-state was successfully used to synthesise CGO without any doping and the CGO doped different percentages Tb^{3+}. The material presents a high crystalline property which was also confirmed by Raman. The time resolved measurement shows the presence of Bi and Zn. It was possible to detect the maximum of the Tb at 542nm with the steady time PL with the finest doping concentration found to be 4%. Increasing the doping concentration caused a continuous decrease in intensity because of the resonant charge transfer of Tb^{3+} ions. The thermoluminescence result with Bi^{3+}, Zn^{2+} and Tb^{3+} revealed the best curve and was fitted with the generalized order kinetic model (GOK). The lowest amount of the filled traps was detected with the sample doped with Bi^{3+} and Zn^{2+}. The energy transfer from Time resolved measurements show a very fast and efficient transfer to the Tb^{3+} sites, indicating the fundamental role in the optical process of the rare earth. Finally, the nature of defeats was generalised by PL and PLE, a broad band of 500nm was seen at 355nm excitation. Intensity was found to increase with sample with Bi and Zn with respect to single Bi. The results indicates that Ca3Ga4O9: Tb^{3+} is a promising material which exhibits potential technological application in the fabrication of optical memory.

References

[1] Ting Wang, Xuhui Xu, Dacheng Zhou, Yong Yang,Jianbei Qiu, and Xue Yu, (2016)Effffect of Defect Distribution on the Optical Storage Properties of Strontium Gallates with a Low-Dimensional Chain Structure. Inorg. Chem., 55, 894−901.

[2] Zhenwei Jia, Chenxu Yuan, Ruiyang Li, Peng Sun, Rui Dong, Yongfu Liu, Lei Wang, Haochuan Jiang and Jun Jiang (2020) Electron–phonon coupling mechanisms of broadband near-infrared emissions from Cr3+ in the $Ca_3Sc2Si_3O_{12}$ garnet Phys. Chem. Chem. Phys., 22, 10343—10350.

[3] Jiaren Du and Dirk Poelman (2019) Facile Synthesis of Mn^{4+}-Activated Double Perovskite Germanate Phosphors with Near-Infrared Persistent Luminescence Nanomaterials, 9(12), 1759.

[4] Shengqiang Liu, Zhizhen Wang, Hao Cai, Zhen Song and Quanlin Liu 2020 Highly efficient near-infrared phosphor LaMgGa11O19:Cr3+. Inorg. Chem. Front., 7, 1467

[5]. Bhargava R N; Gallagher D; Hong X; Nurmikko A; Phys. Rev. Lett., 1994, 72, 416.

[6]. H. Yamamoto and T. Matsuzawa, “Mechanism of long phosphorescence of SrAl2O4:Eu3+2+, Dy3+ and CaAl2O4:Eu3+2+, Nd3+,” J. Lumin. 72-74, 287–289 (1997).

[7]. T. Matsuzawa, Y. Aoki, N. TakEu3+chi, and Y. Murayama, “A new long phosphorescent phosphor with high brightness, SrAl2O4:Eu3+2+Dy3+,” J. Electrochem. Soc. 143(8), 2670–2673 (1996).

[8] T. Matsuzawa, Y. Aoki, N. TakEu3+chi, and Y. Murayama (1996) A New Long Phosphorescent Phosphor with High Brightness, SrAl2 O 4: Eu3+2 + , Dy3 +. J. Electrochem. Soc. 143 2670

[9] Dongjie Liu, Xiaohan Yun, Guogang Li, Peipei Dang, Maxim S. Molokeev, Hongzhou Lian, Mengmeng Shang, and Jun Lin (2020) Enhanced Cyan Emission and Optical Tuning of Ca3Ga4O9:Bi3+ for High-Quality Full-Spectrum White Light-Emitting Diodes Adv. Optical Mater., 8, 2001037.

[10]. Stanic V; Etsell T H; Pierre A C; Mikula R J; Mater. Lett., 1997, 31, 35.

[11]. Yang P; Lü M; Xü D; Zhou G; J. Lumin., 2001, 93, 101

[12] Xu S J; Chua S J; Liu B; Gan L M; Chew C H; Xu G Q; Appl. Phys. Letts., 1998, 73(4), 478.

[13] Xu J; Ji W; J. Mater. Sci. Lett., 1999, 18, 115.

[14] Mengjiao Xu, Luxiang Wang, Dianzeng Jia, Fuhe Le (2015) Luminescence properties and energy transfer investigations of Zn2P2O7: Ce^{3+}, Tb^{3+} phosphor. Journal of Luminescence 158 125–129.

5.1. General Conclusion and Recommendations

In summary, this thesis is a masterpiece for the eco-friendly and high crystalline properties achieved as confirmed by the Raman. The most intriguing is the great and efficient mechanoluminescent (ML) results of the synthesized phosphor. Different methods such as the conventional solid state (SS) and microwave assisted synthesis (MAS) methods has been successfully used to obtain different phosphors of plain $Ca_3Ga_4O_9$ and CaZnOS and their composites with negligible quantities different dopants such as Tb^{3+}, Eu^{3+}, Bi^{3+}, Zn^{2+}. Diverse characterization techniques such as Raman, XRD, EDAX, Steady and Time resolved Luminescence, and ML has been successfully used to check the structural, morphological, optical, and mechanoluminescent properties of the phosphors.

In the first part of the research, only solid-state method was employed for the synthesis of CaZnOS doped and co-doped samples. Experimental and structural characterization (XRD and Raman) as well as DFT calculation on the vibrational properties disclosed the suitable doping site for Tb^{3+} and Eu^{3+}. With the optical studies, further insight on the excitation and emission properties of the doped and co-doped samples were underlined. Particularly, fast non-radiative channels are activated from the defect centers to Tb^{3+} ions, and the same process was obtained from Tb^{3+} to Eu^{3+}.
Hence, the defect centers can be efficiently utilized as sensitizer for the emission at the rare-earth elements site. Since these defects are responsible of the Mechano-luminescence in CaZnOS system, the model can be shifted from optical excitation to impact excitation. The work aimed, to define the model of one of the best mechano-luminescent material developed, as well as outline the basis for further studies based on the energy transfer mechanism among the dopant's centers.

In the second part of the work, two methods such as solid-state and microwave-assisted synthesis routes was carefully utilized for the synthesis of pure CaZnOS and doped with Tb^{3+}. The major aim was to study and compare results obtained by the different methods as well as study the mechanoluminescent of the material with the single impart method with different energies. The different characterization done gave credits to the MAS method for producing results comparable to the SS method and the most interesting is the mechanoluminescent results of the phosphor. Also, by offering a faster reaction time, higher reaction yields, and greater control over reaction conditions, making it an attractive alternative to traditional SS synthesis.

Finally, the persistent luminescence phosphor CGO of pure and doped with different levels of Tb^{3+} with the aim of studying the consequences Tb^{3+} on the material. Solid state method was used in the synthesis

of the LPLP. The Raman analysis confirmed that the phosphor has high crystalline property. The time resolved measurement show the presence of Bi and Zn. It was possible to detect the maximum of the Tb^{3+} at 542nm with the steady time PL with the finest doping concentration found to be 4%. Increasing the doping concentration caused a continuous decrease in intensity because of the resonant charge transfer of Tb^{3+} +ions. The thermoluminescence results with Bi^{3+}, Zn^{2+} and Tb^{3+} revealed the best curve and was fitted with the generalized order kinetic model (GOK). The lowest amount of the filled traps was detected with the sample doped with Bi and Zn. The energy transfer from Time resolved measurements show a very fast and efficient transfer to the Tb^{3+} sites, indicating the fundamental role in the optical process of the rare earth. Finally, the nature of defeats was generalised by PL and PLE, a broad band of 500 nm was seen at 355nm excitation. Intensity was found to increase with sample with Bi and Zn with respect to single Bi. The results indicates that $Ca_3Ga_4O_9$: Tb^{3+} is a promising material which exhibits potential technological application in the fabrication of optical memory.

All the results obtained proved that the broad aim of the research which was to construct eco-friendly and sustainable new phosphors for photonics applications and develop new experimental methods to optimize the industrialization of photonics materials to reduce energy consumption was successfully accomplished.

5.2. Recommendations

It is important to stress that the results obtained throughout study were pleasing and consistent. But there are still few limitations.

This research was done with different methods but was limited to only two such as the SS and the MAS methods and suitable results were realised. These methods have been proven to be suitable synthesis routes from the results of the Raman and other characterizations. Further studies should adopt a different method from the MAS to compare with the SS.

The heating time of the MAS should be increased probably 40min, 50min and 60min since this work was limited to just 10min, 20min and 30min. To see if the content of the unreacted precursors will be reduced.

I Franca Chika, Ugbo awarded scholarships financed with the resources of the National Research and Innovation Operational Program 2014-2020, for the purposes of compliance with the publicity obligations detailed in point 2.2 of Annex XII of EU Regulation n.1303/2013 on "Information and communication measures for the public", have the obligation to insert the official logos of the Program and the wording.

La borsa di dottorato è stata cofinanziata con risorse del
Programma Operativo Nazionale Ricerca e Innovazione 2014-2020 (CCI 2014IT16M2OP005),
Fondo Sociale Europeo, Azione I.1 “Dottorati Innovativi con caratterizzazione Industriale”